

Probing Planck-Scale Physics with High-Frequency Gravitational Waves

Stefano Profumo

*Department of Physics, University of California, Santa Cruz, CA 95064, USA and
Santa Cruz Institute for Particle Physics, University of California, Santa Cruz, CA 95064, USA*

(Dated: March 4, 2026)

We develop a framework for testing quantum gravity through the stochastic gravitational-wave background produced by evaporating near-Planck-mass primordial black holes. Because gravitons free-stream from the emission region without rescattering, they preserve a direct spectral record of the black-hole temperature–mass relation $T(M)$, a relation that is erased for all other Hawking-radiated species by rapid thermalization. We translate six representative phenomenological beyond-semiclassical frameworks (the generalized uncertainty principle, loop quantum gravity, non-commutative geometry, asymptotic safety, string/Hagedorn physics, and tunneling backreaction) into distinct $T(M)$ parametrizations and compute the resulting gravitational wave spectra numerically. Modifications that suppress $T(M)$ shift the spectral peak by up to ten decades in frequency, in some cases into the sensitivity bands of next-generation interferometers or resonant-cavity detectors, while models imposing a hard evaporation cutoff produce distinctive peak morphologies that discriminate between quantum-gravity scenarios. We further discuss the impact of different choices for post-inflationary conditions in the very early universe. We find that the relative spectral displacement between the standard Hawking prediction and any modified model is cosmology-independent, hence spectral shape rather than absolute peak frequency provides the cleanest probe of Planck-scale physics.

I. INTRODUCTION

The marriage of quantum mechanics and general relativity remains one of the most profound open challenges in theoretical physics [1, 2]. While quantum field theory in curved spacetime has provided remarkable insights, most notably through Hawking’s discovery that black holes emit thermal radiation [3, 4] and the associated thermodynamic interpretation of black-hole mechanics [5, 6], a complete, UV-finite quantum theory of gravity remains elusive. The central difficulty is experimental: the natural energy scale of quantum gravitational effects, the Planck scale $E_{\text{Pl}} \sim 10^{19}$ GeV, lies some fifteen orders of magnitude beyond the reach of any conceivable particle accelerator.

A number of indirect observational windows onto quantum gravity have nevertheless been proposed and, in some cases, actively pursued. Searches for Lorentz invariance violation exploit the fact that many quantum-gravity frameworks predict energy-dependent modifications to particle dispersion relations, which accumulate over cosmological distances and can be constrained using high-energy photons from gamma-ray bursts [7, 8] or TeV blazars observed by imaging atmospheric Cherenkov telescopes [9, 10]. Spacetime foam models predict a stochastic distance fuzziness at the Planck scale that can in principle be probed through phase decoherence in interferometers [11, 12] or through the angular blurring of distant point sources [13, 14]. In the gravitational-wave sector, stochastic backgrounds produced during inflation [15, 16] or during a putative bounce in loop quantum cosmology [17, 18] encode quantum-gravitational corrections to the primordial tensor spectrum that future CMB polarization experiments may be able to detect [19]. The generalized uncertainty principle (GUP) framework, orig-

inally motivated by thought experiments in string theory and black-hole physics [20, 21], predicts corrections to atomic spectra, optomechanical oscillators, and scanning tunneling microscopes at levels that are beginning to be constrained [22]. Finally, the observation of near-extremal black holes in X-ray binaries [23] and the direct imaging of black-hole shadows by the Event Horizon Telescope [24, 25] probe the strong-field geometry near horizons and can, in principle, be used to search for quantum corrections to the Kerr metric predicted by specific UV completions of gravity [26].

Despite this breadth of activity, all existing probes are either limited to Planck-suppressed corrections at energies far below E_{Pl} or to qualitative signatures whose connection to a specific microscopic theory is difficult to establish. A direct probe of quantum-gravitational dynamics operating *at* the Planck scale, in a regime where the semiclassical approximation genuinely breaks down, has remained out of reach. The universe itself may, however, provide a laboratory through relics from the Planck epoch: primordial black holes (PBHs) formed in the early universe [27–29] with masses near the Planck scale would have evaporated at temperatures $T \sim T_{\text{Pl}}$, precisely where quantum-gravitational corrections to the standard Hawking law are expected to be largest. As we argue in this paper, the gravitational waves emitted during this process encode a detailed record of those corrections, and that record may be within reach of a new generation of high-frequency gravitational-wave detectors.

In 1974, Hawking demonstrated that black holes are not truly black but emit thermal radiation with a characteristic temperature [3, 4]

$$T_H = \frac{\hbar c^3}{8\pi G M k_B} \approx \frac{10^{-7}}{M/M_\odot} \text{ K}, \quad (1)$$

where M is the black-hole mass. This temperature arises

from quantum vacuum fluctuations near the event horizon and represents a profound synthesis of quantum mechanics (\hbar), gravity (G), and thermodynamics (k_B), a result that has been re-derived in multiple independent frameworks and is widely regarded as one of the most reliable predictions of semiclassical gravity [30, 31]. The corresponding evaporation timescale is [32]

$$\tau_{\text{ev}} \sim \frac{M^3}{M_{\text{Pl}}^2} t_{\text{Pl}} \approx 10^{64} \left(\frac{M}{M_{\odot}} \right)^3 \text{ yr}, \quad (2)$$

where $M_{\text{Pl}} = \sqrt{\hbar c/G} \approx 2.18 \times 10^{-5} \text{ g}$ is the Planck mass and $t_{\text{Pl}} = \sqrt{\hbar G/c^5} \approx 5.4 \times 10^{-44} \text{ s}$ is the Planck time. For a solar-mass black hole, therefore, the evaporation time vastly exceeds the age of the universe, a black hole of mass $M \sim 10^{15} \text{ g}$ evaporates today, while one of mass $M \sim M_{\text{Pl}}$ would have evaporated in a single Planck time, a regime in which the derivation of Eq. (1) ceases to be trustworthy.

Hawking’s derivation rests on the *semiclassical approximation*: the gravitational field is treated as a fixed classical background while matter fields are quantized on top of it. This approximation is well controlled when the spacetime curvature at the horizon, $\mathcal{R} \sim M^{-2}$ in Planck units, is small compared to the Planck scale. As the black hole evaporates, however, the horizon curvature grows without bound, and the semiclassical treatment must eventually break down as $M \rightarrow M_{\text{Pl}}$ [33, 34].

The nature of this breakdown is one of the deepest unsolved problems in theoretical physics [35, 36]. Proposed resolutions span a wide spectrum: the formation of stable or metastable Planck-scale *remnants* that halt evaporation and store the missing information [37, 38]; a unitary evaporation process in which quantum information is gradually transferred to subtle correlations in the outgoing radiation [39, 40]; *firewalls* or other departures from semiclassical physics at the horizon that enforce unitarity at the cost of the equivalence principle for infalling observers [41]; topology-changing transitions in which baby universes or wormholes encode the missing degrees of freedom [42, 43]; and, most recently, the discovery that including gravitational saddle-point contributions (“islands”) in the Euclidean path integral reproduces a unitary Page curve without invoking any exotic horizon physics [44, 45]. While these proposals differ sharply in their microscopic assumptions, they agree on the qualitative conclusion that the canonical $T \propto M^{-1}$ relation in Eq. (1) cannot hold arbitrarily close to the Planck scale. If it did, black holes with $M \ll M_{\text{Pl}}$ would reach temperatures vastly exceeding $T_{\text{Pl}} \sim 10^{32} \text{ K}$, entering a regime where spacetime itself becomes quantum and the notion of a semiclassical geometry loses meaning. Various approaches to quantum gravity, including string theory [46, 47], loop quantum gravity (LQG) [48, 49], asymptotic safety [50], and the GUP [51, 52], all predict modifications to black-hole thermodynamics in precisely this regime, motivating the systematic phenomenological study we undertake below.

The quantum-gravity frameworks surveyed in Sec. II share a common phenomenological implication: the standard semiclassical relation $T \propto M^{-1}$ must be modified once black-hole evaporation probes Planckian energies. The nature of the correction depends on the underlying theory, but the possibilities can be organized according to the qualitative behavior of $T(M)$ as $M \rightarrow M_{\text{Pl}}$.

In string-theoretic constructions, quantum and higher-derivative corrections to the near-horizon geometry modify the thermodynamic relations in a controlled way at small mass [53, 54], while Hagedorn-density-of-states arguments suggest a transition to a string-dominated phase with a maximal temperature once the string scale is reached. In GUP models, the deformed uncertainty relation leads to corrections that can be organized as a systematic expansion in M_{Pl}/M ,

$$T(M) = \frac{1}{8\pi M} \left[1 - \beta \left(\frac{M_{\text{Pl}}}{M} \right) + \mathcal{O} \left(\frac{M_{\text{Pl}}}{M} \right)^2 \right], \quad (3)$$

where β is a dimensionless model-dependent parameter [55, 56]. Higher-order terms in this series can drive $T(M)$ to a maximum before forcing it back to zero at a finite remnant mass, generically implying altered entropy–area relations and long-lived Planck-scale remnants [38, 51, 57]. LQG- and noncommutative-geometry-inspired solutions share this qualitative endpoint behavior, while tunneling and backreaction corrections provide a conservative, minimal-assumption realization of the same physics.

In each case the deviation from the Hawking law is confined to the final stages of evaporation, leaving the well-tested (at least theoretically!) large-mass behavior intact. In the following section we translate these theoretical possibilities into a set of concrete, phenomenologically distinct $T(M)$ parametrizations suitable for computing the gravitational-wave emission spectrum.

Among all particle species produced by Hawking evaporation, gravitons occupy a privileged role as carriers of spectral information. Every other species, such as photons, neutrinos, and quarks, undergoes rapid thermalization in the primordial plasma once emitted, erasing the imprint of the black-hole temperature on timescales set by the interaction rate $\Gamma_{\text{int}} \sim \alpha T^2/M_{\text{Pl}}$, where α is a representative coupling strength. Thermalization is therefore effective at all temperatures below $T \sim M_{\text{Pl}}/\alpha$, which for Standard Model couplings ($\alpha \lesssim 10^{-2}$) is at least two orders of magnitude above the Planck temperature itself, comfortably encompassing the entire evaporation history for the black-hole masses of interest here. Gravitons, interacting only gravitationally with strength $\sim T/M_{\text{Pl}} \ll 1$, free-stream from the point of emission without further scattering [58, 59]. Their spectrum therefore preserves a direct, undistorted record of $T(M)$ throughout the evaporation, making the gravitational-wave background a uniquely clean probe of near-Planckian black-hole thermodynamics.

For a black hole at temperature T , the power radiated in any particle species of spin s follows a Stefan–Boltzmann

law weighted by spin-dependent greybody factors that account for the scattering and partial reflection of quanta by the curved spacetime near the horizon [31, 32, 60]. The emission spectrum is thermal and strongly peaked at frequencies $f \sim T(M)/h$, so the entire evaporation history maps onto a characteristic frequency band in the emitted graviton spectrum. For $M \sim M_{\text{Pl}}$ the standard Hawking relation gives $T \sim T_{\text{Pl}}$, implying emission frequencies

$$f_{\text{em}} \sim \frac{k_B T_{\text{Pl}}}{h} \sim 10^{32} \text{ Hz}. \quad (4)$$

After cosmological redshifting by a factor $(1 + z_{\text{em}})^{-1}$ set by the epoch of evaporation, these ultra-high frequencies map onto a present-day band potentially spanning the MHz–THz regime, depending on the reheating temperature and expansion history, as we explore below in Sec. V.

A population of light PBHs with masses $M \sim 10^{-1} - 10^2 M_{\text{Pl}}$, formed in the early Universe and evaporating prior to Big Bang Nucleosynthesis, would produce a stochastic gravitational-wave background (SGWB) through their cumulative incoherent graviton emission [61, 62]. Unlike SGWBs from compact binary coalescences or inflation, this background originates from the quantum evaporation of horizons and probes physics at energies approaching the Planck scale. Its spectral shape is sensitive to $T(M)$, its overall amplitude to the PBH abundance and mass distribution at formation, and its peak frequency to the cosmological history between evaporation and today, three largely independent handles that together make the SGWB a powerful multi-parameter diagnostic of Planck-scale physics.

The direct detection of gravitational waves by LIGO and Virgo [63, 64] has established gravitational-wave astronomy as a precision probe of the Universe, but existing and planned detectors cover only a narrow slice of the accessible frequency spectrum. Ground-based interferometers (LIGO, Virgo, KAGRA, and their third-generation successors ET and CE) are sensitive in the $\sim 10 - 10^4$ Hz band [65], the space-based LISA mission will open the $\sim 10^{-4} - 10^{-1}$ Hz window, and pulsar timing arrays probe nHz frequencies [66]. The regime above $\sim 10^5$ Hz remains essentially unexplored, despite the fact that a variety of well-motivated early-Universe processes, including first-order phase transitions, cosmic string networks, and, as argued here, PBH evaporation, are expected to produce signals in this band.

Bridging this gap has become an active area of research. Proposed high-frequency detection strategies exploit the coupling of gravitational waves to electromagnetic fields or mechanical degrees of freedom, and include: inverse-Gertsenshtein conversion of gravitational waves into photons in strong magnetic fields [67–69]; resonant electromagnetic cavities that enhance this conversion for narrowband signals [70, 71]; and optomechanical or levitated-sensor approaches sensitive to rapid spacetime oscillations [72]. While none of these has yet reached astrophysically relevant sensitivity, they collectively demon-

strate that the MHz–GHz frontier is experimentally accessible in principle, and rapid progress in quantum sensing and superconducting cavity technology is narrowing the gap between current performance and the targets required to probe early-Universe sources.

This frequency window is precisely where signals from near-Planck-mass PBH evaporation are expected to appear after cosmological redshifting, making the high-frequency GW frontier a natural, and, we argue, uniquely motivated, arena for testing quantum gravity through an astronomical observable.

A detection of spectral features in the high-frequency SGWB inconsistent with the standard Hawking prediction would constitute a qualitatively new form of empirical access to quantum-gravitational physics. The key advantage of this probe over alternatives such as searches for Lorentz invariance violation [9, 73], spacetime foam-induced decoherence [14], or dispersion-relation modifications [74] is interpretive clarity: Hawking evaporation provides a framework in which the large-mass behavior is firmly established semiclassically, deviations at small mass can be systematically parameterized, and any inferred departure from $T \propto M^{-1}$ points unambiguously to quantum-gravitational dynamics at the horizon scale rather than to a generic violation of low-energy effective field theory.

Connecting this signal to observation requires confronting the cosmological redshifting of the emitted gravitons, which introduces both a challenge and an opportunity. The present-day spectrum depends not only on $T(M)$ but also on the expansion history between evaporation and today, specifically, the epoch at which evaporation completes, the reheating temperature and entropy content of the radiation bath, the fractional PBH contribution to the total energy density, and the possible presence of nonstandard expansion phases such as early matter domination or kination. Different cosmological scenarios can shift the spectral peak by many decades in frequency and alter the overall amplitude by orders of magnitude. Rather than treating this as an irreducible systematic, however, one can exploit the fact that the spectral shape, peak frequency, and amplitude encode *correlated* information about both $T(M)$ and the cosmological environment: the redshift problem, properly framed, becomes a source of additional diagnostic power.

The remainder of this paper is organized as follows. Section II surveys the quantum-gravity frameworks that motivate modifications to the Hawking temperature–mass relation, including the GUP, noncommutative geometry, loop quantum gravity, asymptotic safety, string theory, and tunneling/backreaction corrections. Section III translates these motivations into a set of concrete, phenomenologically distinct $T(M)$ parametrizations and derives their qualitative consequences for the evaporation history and graviton emission spectrum. Section IV describes the production of a stochastic gravitational-wave background from light PBHs, establishes why the signal is stochastic in nature, and presents the integral formula connecting

the instantaneous graviton spectrum to the present-day $\Omega_{\text{GW}}(f_0)$ (see eq. (23) for a definition thereof). Section V treats the cosmological redshifting problem, covering the standard radiation-dominated mapping, the realistic upper bound set by the reheating temperature, and the modifications arising from early matter domination, kination, and nonstandard reheating histories. Section VI presents the numerical GW spectra for all six modified-temperature models across a range of parameters and initial masses, compares them with detector sensitivity envelopes, and discusses the experimental requirements for resonant-cavity detection. Section VII summarizes our conclusions and outlines directions for future work. Throughout, we retain all fundamental constants (\hbar , c , G , k_B) explicitly in dimensional expressions; the numerical spectra in Sec. VI are computed in the dimensionless units defined in Appendix A, with all masses measured in units of M_{Pl} .

II. QUANTUM-GRAVITY CANDIDATES AFFECTING EVAPORATION NEAR M_{Pl}

As the black-hole mass approaches the Planck scale, curvature invariants at the horizon become large, quantum fluctuations of the geometry are no longer parametrically suppressed, and the notion of a fixed classical background ceases to be reliable. Any complete theory of quantum gravity must specify how the temperature–mass relation $T(M)$ is modified in this regime. While no fully predictive theory is currently available, a number of well-studied frameworks provide qualitative guidance, and their qualitative predictions for $T(M)$ near M_{Pl} are sufficiently distinct to motivate a systematic phenomenological survey. We outline each in turn.

A. Generalized Uncertainty Principle

The GUP incorporates a minimal measurable length into the structure of quantum mechanics by deforming the Heisenberg relation to include Planck-suppressed corrections [21, 51], leading to altered dispersion relations and modified phase-space structure at high energies. Applied to black-hole thermodynamics, these deformations modify the relation between horizon size and characteristic emission wavelength, generically driving $T(M)$ to a maximum before forcing it back toward zero as M approaches a minimum value of order M_{Pl} [55, 56]. This behavior regulates the semiclassical runaway and is commonly interpreted as signaling the formation of a stable or metastable Planck-scale remnant [38, 51].

B. Noncommutative Geometry

In noncommutative-geometry–inspired models, space-time coordinates satisfy nontrivial commutation relations,

effectively smearing point-like sources over a minimal length scale [75]. Black-hole solutions constructed in this framework replace the classical singularity with a regular core, and the horizon structure is modified at small radius. The resulting Hawking temperature reaches a finite maximum and then decreases to zero at a minimal mass [76], qualitatively similar to the GUP outcome but with a temperature suppression that is quadratic in M_{min}/M rather than the square-root suppression characteristic of many LQG constructions (see below). This difference in the functional form of $T(M)$ near M_{min} is directly reflected in the width and asymmetry of the resulting gravitational-wave spectrum.

C. Loop Quantum Gravity and Polymerized Black Holes

Loop quantum gravity provides a nonperturbative, background-independent quantization of spacetime geometry in which areas and volumes acquire discrete spectra. Effective black-hole solutions inspired by LQG replace the classical singularity with a quantum region governed by polymerized geometry [77, 78], and many such constructions predict a transition to a “Planck star”—a compact, Planck-density object whose evaporation history differs markedly from the standard picture [79]. The temperature either vanishes smoothly or remains finite as $M \rightarrow M_{\text{min}}$, suppressing the Hawking runaway and producing an extended or halted evaporation phase whose GW signature we compute in Sec. III.

D. Asymptotic Safety and Renormalization-Group Improvements

In the asymptotic safety scenario, gravity possesses a nontrivial ultraviolet fixed point that renders Newton’s constant scale-dependent at high energies [80, 81]. Renormalization-group–improved black-hole solutions derived in this framework exhibit a running $G(k) \sim G_0/(1 + \xi G_0 k^2)$ near the horizon, where $k \sim M^{-1}$ is the relevant momentum scale [82]. The resulting $T(M)$ relation deviates from the semiclassical form once the running becomes important, typically approaching a finite maximum temperature and yielding a modified evaporation endpoint. Unlike the GUP and NC scenarios, asymptotic safety does not introduce a minimal mass per se, but rather a smooth infrared–ultraviolet interpolation that softens the late-time luminosity.

E. String-Theoretic Considerations and the Hagedorn Temperature

String theory provides a UV-complete framework in which black holes transition into highly excited string states once their mass approaches the string scale [83].

The exponentially growing density of string states implies a maximal (Hagedorn) temperature T_H at which thermodynamic systems absorb energy without further heating, suggesting that black-hole evaporation may be regulated by a smooth crossover from a black-hole phase to a string-dominated phase [84, 85]. Unlike the remnant-forming scenarios above, this predicts a *limiting* rather than a vanishing temperature: $T(M) \rightarrow T_H$ as $M \rightarrow 0$, with T_H set by the string tension. The resulting graviton spectrum has a qualitatively distinct high-frequency cutoff whose location encodes the string scale directly.

F. Tunneling and Backreaction Corrections

A conceptually distinct modification arises from enforcing energy conservation during the emission process. In the original semiclassical derivation, Hawking radiation is computed on a fixed background, ignoring the fact that each emitted quantum reduces the black-hole mass and thereby modifies the geometry seen by subsequent quanta. Interpreting Hawking radiation as a tunneling process across the horizon [86] enforces this energy conservation explicitly: the emission of a quantum of energy ω shifts the black-hole mass from M to $M - \omega$, and the corrected tunneling rate

$$\Gamma(\omega) \propto \exp[\Delta S_{\text{BH}}(M - \omega) - \Delta S_{\text{BH}}(M)] \quad (5)$$

deviates from exact thermality at order ω/M . To leading order, these backreaction corrections reduce the effective temperature relative to the Hawking value [87, 88], providing a conservative lower bound on the magnitude of Planck-scale modifications that does not invoke any new microscopic degrees of freedom. In this sense, tunneling corrections serve as a minimal benchmark against which the more radical modifications of the preceding subsections can be compared.

G. Shared Features and Phenomenological Organization

Despite their different microscopic origins, the frameworks above share three qualitative features that are directly relevant for gravitational-wave phenomenology. First, all introduce a characteristic mass scale—a minimal length, a running coupling scale, a string tension, or a remnant mass—that regulates the semiclassical divergence of $T(M)$ as $M \rightarrow M_{\text{P1}}$. Second, the nature of this regulation falls into two broad classes: *limiting-temperature* models (plateau and Hagedorn), in which T saturates at a finite value, and *cooling* models (GUP, NC, LQG, tunneling), in which T reaches a maximum and subsequently decreases. Third, the corrections to other thermodynamic quantities—entropy, heat capacity, and luminosity—follow from the same physics and can significantly prolong or arrest the final evaporation phase, with direct consequences for the duration and spectral content

of graviton emission. These shared features motivate the phenomenological parametrizations of $T(M)$ introduced in Sec. III, which are designed to capture the essential physics of each class in a form amenable to quantitative gravitational-wave calculations.

III. MODIFIED BLACK-HOLE TEMPERATURE–MASS RELATIONS

A. Standard Hawking law

In semiclassical gravity, a stationary black hole radiates thermally at the Hawking temperature determined by its surface gravity κ ,

$$T_{\text{H}} = \frac{\hbar \kappa}{2\pi k_{\text{B}} c}, \quad (6)$$

a relation that holds for generic horizons and underlies the identification of black holes as thermodynamic systems [4, 5, 30]. For a four-dimensional, asymptotically flat Schwarzschild black hole,

$$\kappa = \frac{c^4}{4GM}, \quad T_{\text{H}}(M) = \frac{\hbar c^3}{8\pi G k_{\text{B}} M} \equiv \frac{1}{8\pi} \frac{M_{\text{P1}}^2 c^2}{k_{\text{B}} M}, \quad (7)$$

so that $T_{\text{H}} \propto M^{-1}$. In convenient numerical form,

$$T_{\text{H}} \simeq 6.17 \times 10^{-8} \text{ K} \left(\frac{M_{\odot}}{M} \right) \simeq 1.06 \text{ GeV} \left(\frac{10^{13} \text{ g}}{M} \right), \quad (8)$$

where the second expression is particularly useful for primordial black holes. This scaling implies that as a black hole evaporates its temperature rises monotonically, driving an increasingly rapid late-time evolution.

The corresponding semiclassical mass-loss rate is

$$\frac{dM}{dt} = -\frac{\alpha(M)}{M^2}, \quad (9)$$

where $\alpha(M)$ encodes the effective number of emitted species and the relevant greybody factors; in the high-temperature limit where all Standard Model degrees of freedom are accessible, $\alpha(M)$ is approximately constant between threshold crossings [32, 60]. Integrating Eq. (9) gives

$$\tau_{\text{evap}}(M_0) \simeq \frac{M_0^3}{3\alpha} \propto M_0^3, \quad (10)$$

which in conventional units yields

$$\tau_{\text{evap}} \simeq 4 \times 10^{-28} \text{ s} \left(\frac{M_0}{1 \text{ g}} \right)^3 \simeq 4 \times 10^{17} \text{ s} \left(\frac{M_0}{5 \times 10^{14} \text{ g}} \right)^3 \quad (11)$$

up to $\mathcal{O}(1)$ factors [28, 60]. The instantaneous emission spectrum is approximately thermal at temperature $T_{\text{H}}(M)$, with spin-dependent greybody factors encoding propagation through the curved spacetime outside the

horizon [32]. Graviton emission is strongly suppressed at large mass but becomes appreciable in the final stages as the temperature rises, making the high-frequency tail of the SGWB directly sensitive to the late-time behavior of $T(M)$ [32, 61].

An additional consideration is black-hole rotation. For Kerr black holes the Hawking temperature is reduced relative to the Schwarzschild value at fixed mass, while the greybody factors become strongly spin- and mode-dependent. Bosonic radiation is further enhanced through superradiant amplification for modes satisfying $\omega < m\Omega_H$, where Ω_H is the horizon angular velocity [89–91], so rapidly spinning black holes radiate a substantially larger fraction of their power in high-spin channels, including gravitons, and spin down efficiently during evaporation [91, 92]. For primordial black holes, whose initial spin distribution is model dependent, rotation can therefore significantly affect both the amplitude and spectral shape of the high-frequency SGWB [28, 93]. We defer a systematic treatment of the Kerr case to future work and focus here on the non-rotating limit, which captures the essential physics of the temperature–mass modifications of interest.

Equation (7) provides the baseline against which any Planck-scale modification is defined. In the remainder of this section we introduce representative deformations that capture qualitatively distinct possibilities for how the semiclassical evaporation law may be regulated as $M \rightarrow M_{\text{Pl}}$.

B. Plateau and Hagedorn-like models

A common expectation in UV-complete or UV-regulated frameworks is that the divergent rise of the Hawking temperature is softened near the fundamental scale. In string theory the exponentially growing density of states allows thermodynamic systems to approach a limiting (Hagedorn) temperature, suggesting a crossover from a black-hole phase to a string-dominated regime [83, 84]. Motivated by this behavior, we model the approach to a maximal temperature through a smooth saturation of $T(M)$:

$$T_{\text{plat}}(M) = \frac{1}{8\pi} \frac{M_{\text{Pl}}^2}{\sqrt{M^2 + M_c^2}}, \quad (12)$$

where M_c is a characteristic crossover mass. For $M \gg M_c$, Eq. (12) reduces to the standard Hawking law; for $M \ll M_c$ it asymptotes to a finite maximal temperature

$$T_{\text{max}} = \frac{1}{8\pi} \frac{M_{\text{Pl}}^2}{M_c}. \quad (13)$$

A related parametrization that more directly mimics a Hagedorn-like limiting temperature is

$$T_{\text{Hag}}(M) = \frac{T_H}{1 + \left(\frac{M}{M_H}\right)^p}, \quad T_H \equiv \frac{1}{8\pi} \frac{M_{\text{Pl}}^2}{M_H}, \quad (14)$$

with $p > 0$ controlling the sharpness of the crossover; for $M \gg M_H$ this reproduces $T \propto M^{-1}$, while for $M \ll M_H$ the temperature saturates to T_H [84, 85]. Both Eqs. (12) and (14) should be regarded as effective descriptions of UV-regulated evaporation rather than first-principles predictions; the crossover scales M_c and M_H encode the onset of new degrees of freedom and control the location of spectral features in the graviton background.

The effect on the evaporation history is immediate. The standard Hawking luminosity $L \propto M^{-2}$ implies a runaway at late times. Once T saturates in a plateau/Hagedorn model, however, $L \propto M^2 T_{\text{max}}^4$ and the evaporation rate slows dramatically. Absent an additional termination mechanism, this prolonged low-luminosity phase can produce quasi-stable Planck-scale relics whose lifetimes are parametrically enhanced relative to the semiclassical expectation [38, 57].

C. Cooling models and post-peak temperature decrease

A qualitatively distinct possibility is that $T(M)$ reaches a maximum at a finite mass and subsequently *decreases*, so that the late stages of evaporation are characterized by progressively softer emission. A convenient parametrization is

$$T_{\text{cool}}(M) = \frac{1}{8\pi} \frac{M_{\text{Pl}}^2 M}{M^2 + M_c^2}, \quad (15)$$

where M_c sets the peak-temperature mass. For $M \gg M_c$, Eq. (15) reduces to $T \propto M^{-1}$; for $M \ll M_c$ it gives $T \propto M$, so the temperature vanishes linearly as $M \rightarrow 0$. The peak occurs at $M = M_c$ with

$$T_{\text{max}} = \frac{1}{16\pi} \frac{M_{\text{Pl}}^2}{M_c}. \quad (16)$$

This qualitative behavior—a maximum followed by a decrease—arises naturally in GUP frameworks, noncommutative geometry, and LQG-inspired constructions (as discussed in Sec. II), making Eq. (15) a useful phenomenological representative of that entire class.

The dynamical consequences are substantial: for $M \ll M_c$ the luminosity scales as $L \propto M^6$, so the evaporation rate slows dramatically and the black hole either asymptotes to a long-lived remnant or undergoes an extended phase of low-temperature emission [38, 57]. For gravitational-wave phenomenology, because the hardest graviton emission occurs at intermediate masses $M \sim M_c$, the SGWB in cooling scenarios exhibits a pronounced peak at the frequency set by T_{max} , followed by a rapid high-frequency falloff—a spectral shape qualitatively distinct from both the standard Hawking case and the plateau/Hagedorn models.

D. GUP-corrected, noncommutative, and LQG-inspired forms

The frameworks reviewed in Sec. II motivate a class of $T(M)$ relations that share the feature of a minimum mass M_{\min} below which evaporation ceases. The key phenomenological distinction among them is the functional form of $T(M)$ as $M \rightarrow M_{\min}^+$, which controls the width and asymmetry of the resulting GW spectral peak.

For GUP-based models, the correction to the Hawking temperature can be written schematically as

$$T_{\text{GUP}}(M) = \frac{1}{8\pi M} \left[1 - \mathcal{O}\left(\frac{M_{\text{Pl}}}{M}\right)^2 \right], \quad (17)$$

with higher-order terms driving T to zero at a finite remnant mass [55, 56]. A cleaner parametrization that captures this behavior exactly and enforces a minimal mass is

$$T_{\text{GUP}}(M) = \frac{A}{2M/\beta} \left[1 - \sqrt{1 - \frac{\beta}{M^2}} \right], \quad M \geq \sqrt{\beta}, \quad (18)$$

where $\beta > 0$ is the deformation parameter and $\sqrt{\beta}$ plays the role of the remnant mass.

The LQG-inspired and noncommutative-geometry forms are distinguished by the power with which T vanishes near M_{\min} :

$$T_{\text{LQG}}(M) = \frac{A}{M} \sqrt{1 - \left(\frac{M_{\min}}{M}\right)^2}, \quad M \geq M_{\min}, \quad (19)$$

$$T_{\text{NC}}(M) = \frac{A}{M} \left[1 - \left(\frac{M_{\min}}{M}\right)^2 \right], \quad M \geq M_{\min}. \quad (20)$$

In both cases $T \rightarrow 0$ as $M \rightarrow M_{\min}$, but the LQG suppression is $\propto (M - M_{\min})^{1/2}$ while the NC suppression is $\propto (M - M_{\min})$, a quadratic rather than square-root vanishing. This difference is directly imprinted on the GW spectrum: the NC spectral peak is narrower and more sharply defined than its LQG counterpart at comparable M_{\min} , providing a potential morphological discriminant between the two frameworks.

E. Tunneling and backreaction-based corrections

Interpreting Hawking radiation as a quantum tunneling process across the horizon [86] enforces energy conservation explicitly: the emission of a quantum of energy ω shifts the black-hole mass from M to $M - \omega$, modifying the geometry seen by the tunneling particle. The corrected emission rate is

$$\Gamma(\omega) \propto \exp[\Delta S_{\text{BH}}(M - \omega) - \Delta S_{\text{BH}}(M)], \quad (21)$$

which deviates from exact thermality at order ω/M and can be recast as an effective temperature suppression,

$$T_{\text{eff}}(M) = T_{\text{H}}(M) \left[1 - \mathcal{O}\left(\frac{T_{\text{H}}}{M}\right) \right]. \quad (22)$$

These corrections are formally suppressed by M_{Pl}/M but become $\mathcal{O}(1)$ when $M \sim M_{\text{Pl}}$ [87, 88], producing a softened and prolonged final evaporation phase that is qualitatively similar to the cooling scenarios above. Unlike GUP or NC models, tunneling corrections require no new microscopic degrees of freedom and in this sense provide a *minimal* benchmark for Planck-scale modifications of $T(M)$.

F. Comparative summary and physical interpretation

The models introduced above can be organized into two phenomenologically distinct classes according to their behavior as $M \rightarrow 0$ (or $M \rightarrow M_{\min}$):

Limiting-temperature models (plateau, Hagedorn): $T(M)$ saturates at a finite value T_{max} set by a new fundamental scale. The evaporation rate slows at late times, redistributing power toward lower frequencies relative to standard Hawking.

Cooling models (GUP, NC, LQG, tunneling): $T(M)$ reaches a maximum at an intermediate mass and then decreases toward zero, concentrating graviton emission in a finite frequency window and producing a sharply peaked $\Omega_{\text{GW}}(f)$ with a steep high-frequency cutoff.

Within the cooling class, the sharpness of the spectral peak is further controlled by the functional form of T near M_{\min} : the NC quadratic suppression yields a narrower peak than the LQG square-root suppression, and the tunneling correction—the most conservative of the group—yields the broadest. These differences, summarized in Figs. 1 and 2, translate directly into distinctive spectral morphologies in $\Omega_{\text{GW}}(f_0)$ that we compute in Sec. VI. The logarithmic representation emphasizes the shared semiclassical asymptotics and makes clear that deviations from the Hawking law are confined to a narrow mass interval near M_{Pl} . The linear-scale plot highlights the qualitative distinctions—peak heights, the onset of cooling, and the presence of a minimum mass—that translate into the spectral features discussed in what follows (Sec. VI in particular).

Figure 3 illustrates how the $T(M)$ classes map onto evaporation histories $M(t)$. In the standard Hawking picture, most of the lifetime is spent near M_0 , followed by a brief terminal plunge as the temperature diverges. Plateau/Hagedorn models stretch this final phase by suppressing the luminosity growth; cooling models extend it further by allowing the temperature—and hence the power—to decrease at late times, producing an extended low-mass tail. Models where $T \rightarrow 0$ at a finite M_{\min} produce trajectories that asymptote to a nonzero mass, mimicking remnant formation on cosmological timescales.

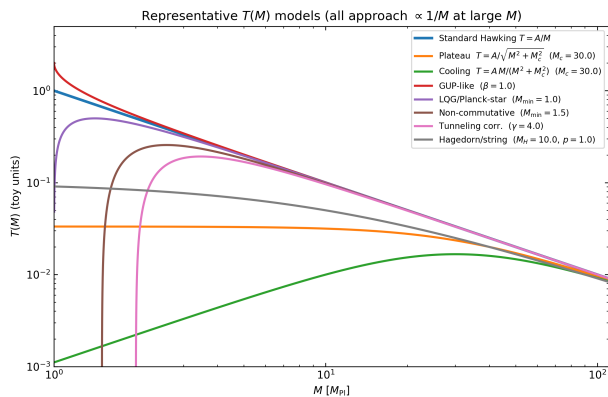


FIG. 1. Representative temperature–mass relations $T(M)$ for the modified black-hole evaporation models considered in this work, shown on logarithmic axes. All curves asymptote to the standard Hawking behavior $T \propto M^{-1}$ at large mass while exhibiting qualitatively distinct behavior near the Planck scale: plateau/Hagedorn-like saturation, cooling (post-peak decrease), GUP-, LQG-, and noncommutative-geometry–inspired forms with minimum masses, and tunneling/backreaction corrections.

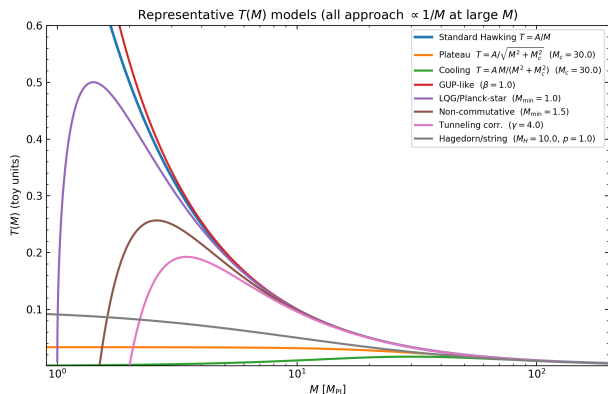


FIG. 2. Same as Fig. 1 on linear axes, highlighting the relative ordering of peak temperatures, the presence or absence of maxima, and the suppression or termination of evaporation near a minimum mass.

These qualitative differences in $M(t)$ map directly onto the emission history and hence the present-day GW spectrum: a rapid plunge concentrates power at the highest frequencies, while a stalled or prolonged tail redistributes it toward lower frequencies and reduces the peak amplitude,

IV. GRAVITATIONAL-WAVE PRODUCTION FROM LIGHT PBHS

Primordial black holes with masses far below the astrophysical scale produce gravitational radiation through several distinct mechanisms during their evaporation. Because PBHs form with a broad spatial distribution,

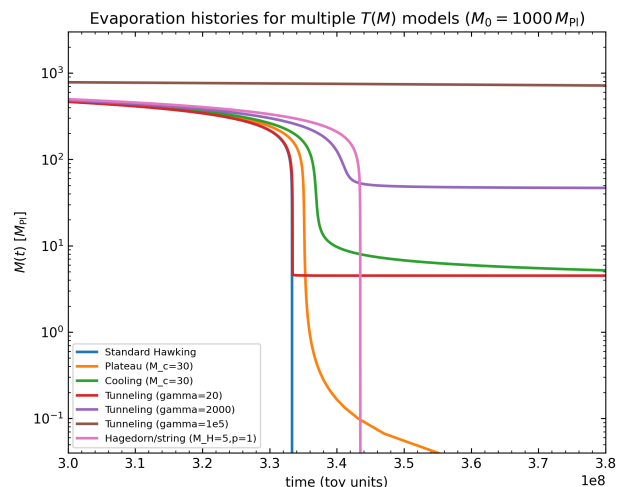


FIG. 3. Illustrative evaporation histories $M(t)$ for initial mass $M_0 = 10^3 M_{\text{Pl}}$ in several modified $T(M)$ scenarios. The figure shows how modified models can (i) delay the late-stage evolution, (ii) produce a prolonged low-mass tail, or (iii) effectively arrest evaporation at a finite remnant mass. Time is shown in the dimensionless units of Appendix A.

evaporate independently, and emit Hawking quanta with random phases, their cumulative GW output is inherently incoherent, giving rise to a SGWB rather than a resolvable transient signal. In this section we describe the relevant emission processes, establish the stochastic nature of the signal, and present the integral formula connecting the evaporation physics to the observable spectral energy density $\Omega_{\text{GW}}(f_0)$.

A. Emission mechanisms

a. Direct graviton emission. In the semiclassical description of Hawking evaporation, black holes emit all particle species with masses below the instantaneous temperature, including gravitons [32, 60]. Graviton emission is suppressed relative to lower-spin species at low temperatures due to the higher angular-momentum barrier in the spin-2 greybody factors, but becomes an appreciable fraction of the total radiated power as the temperature approaches M_{Pl} [32]. Because gravitons interact only gravitationally, they free-stream from the horizon without further scattering (as established in Sec. I), preserving a direct record of $T(M)$ in the emitted spectrum.

b. Secondary gravitational-wave production. GWs can also be generated indirectly through the decay, annihilation, or hadronization of energetic particles produced alongside the direct Hawking quanta [61]. Relativistic particle cascades and the decay of heavy intermediates can source tensor perturbations in the surrounding plasma. These secondary processes are typically subdominant to direct graviton emission at the highest frequencies, but can broaden the GW spectrum and introduce model-

dependent features tied to the particle content of the theory. We neglect this emission mechanism in what follows.

c. Evaporation-induced cosmological dynamics. If PBHs constitute a non-negligible fraction of the total energy density prior to evaporation, their disappearance injects entropy and radiation into the primordial plasma, modifying the subsequent expansion history [28, 94]. This energy injection does not directly source coherent GWs, but it alters the redshifting and dilution of previously emitted gravitons, making the final observed spectrum sensitive to the cosmological environment at the time of evaporation. We treat this dependence in detail in Sec. V.

B. Stochastic nature and spectral characterization

The observable quantity is the spectral energy density

$$\Omega_{\text{GW}}(f) \equiv \frac{1}{\rho_c} \frac{d\rho_{\text{GW}}}{d \ln f}, \quad (23)$$

where ρ_c is the critical energy density. This quantity is insensitive to the detailed spatial distribution of individual PBHs and instead encodes information about the PBH mass function, the evaporation dynamics, and the temperature–mass relation $T(M)$ [61, 62]. The PBH evaporation SGWB is sharply peaked at high frequencies, reflecting the microscopic energy scale of the emission process, which distinguishes it morphologically from the SGWBs produced by inflation or compact binary populations and makes it a distinctive target for high-frequency GW searches.

C. Energy-density spectrum and its dependence on $T(M)$

For a population of PBHs evaporating over a range of cosmic times, the present-day $\Omega_{\text{GW}}(f_0)$ is obtained by integrating the instantaneous graviton emission over the mass evolution and the cosmological expansion. At the level of a single black hole, the instantaneous graviton spectrum is approximately thermal,

$$\frac{d^2 E_{\text{GW}}}{dt d\omega} \simeq \sum_{\ell, m} \frac{\Gamma_{\ell m}^{(2)}(\omega, M)}{2\pi} \frac{\omega}{\exp[\omega/T(M)] - 1}, \quad (24)$$

where $\Gamma_{\ell m}^{(2)}$ are the spin-2 greybody factors [32]. The emission is peaked at $\omega_{\text{peak}} \sim T(M)$, establishing a direct correspondence between $T(M)$ and the frequencies populated at each stage of evaporation.

Redshifting the emitted gravitons and integrating over the evaporation history gives

$$\frac{d\rho_{\text{GW}}}{d \ln f_0} = \int dt \left(\frac{a(t)}{a_0} \right)^4 \frac{d^2 E_{\text{GW}}}{dt d \ln f} \Big|_{f=f_0 a_0/a(t)}, \quad (25)$$

where $a(t)$ is the scale factor and f_0 the observed frequency today. Equation (25) makes explicit the two-fold dependence of $\Omega_{\text{GW}}(f_0)$ on $T(M)$: its functional form determines which emission epochs dominate the GW production (and hence the characteristic frequency scale), while the duration and intensity of the high-temperature phase control the overall efficiency. The sensitivity of the SGWB to Planck-scale modifications of $T(M)$ therefore operates through both the peak frequency and the spectral shape, complementing constraints derived from particle emission, Big Bang nucleosynthesis, and the effective number of relativistic species.

V. COSMOLOGICAL REDSHIFTING AND EXPANSION HISTORY

The present-day frequency and amplitude of the gravitational-wave background depend not only on the emission process studied in Secs. III–IV but on the entire expansion history between PBH evaporation and today. This section establishes the emission-to-observation frequency mapping, derives the realistic upper bound imposed by reheating on the maximum relevant redshift, and analyses how nonstandard expansion phases alter the predicted spectrum.

A. Emission–observation frequency mapping

A graviton emitted at cosmic time t_{em} with physical frequency f_{em} is observed today at frequency

$$f_0 = \frac{a(t_{\text{em}})}{a_0} f_{\text{em}} = \frac{f_{\text{em}}}{1 + z_{\text{em}}}, \quad (26)$$

where $a(t)$ is the scale factor and z_{em} the redshift at emission. For Hawking-radiated gravitons the characteristic emission frequency is set by the instantaneous black-hole temperature,

$$f_{\text{em}} \sim \frac{T(M)}{2\pi}, \quad (27)$$

up to order-unity factors from the greybody spectrum. Together, Eqs. (26)–(27) make explicit that f_0 is sensitive to *both* $T(M)$ and the cosmological history encoded in z_{em} .

During radiation domination, entropy conservation fixes the redshift–temperature relation

$$1 + z(T) \equiv \frac{a_0}{a(T)} = \left(\frac{g_{*S}(T)}{g_{*S,0}} \right)^{1/3} \frac{T}{T_0}, \quad (28)$$

where $T_0 \simeq 2.73$ K is the present CMB temperature and g_{*S} counts the effective entropy degrees of freedom [58, 59]. Equation (28) is exact so long as the expansion is radiation dominated and no entropy is injected into the thermal bath. When PBH evaporation occurs during radiation

domination without significantly perturbing the background, it provides a straightforward mapping between emission and observation.

However, Eq. (28) is often extrapolated formally to arbitrarily high temperatures, yielding a redshift $1+z \sim 10^{31}$ at $T \sim T_{\text{Pl}}$. This extrapolation implicitly assumes that radiation domination persists to those temperatures and that the notion of a thermal plasma remains well defined; both assumptions fail in realistic early-Universe scenarios, as discussed in the following subsection.

B. Reheating and the maximal cosmological redshift

In standard cosmology the radiation-dominated era begins only after reheating at temperature T_{RH} ; prior to reheating, the Universe may be dominated by the oscillating inflaton field or by another form of nonrelativistic energy density. Gravitational waves produced before the onset of radiation domination continue to redshift, but the scale-factor–temperature relation (28) no longer applies. The maximal physically meaningful redshift for GW modes emitted at or before reheating is therefore

$$1 + z_{\text{RH}}^{\text{max}} \simeq \left(\frac{g_{*S}(T_{\text{RH}})}{g_{*S,0}} \right)^{1/3} \frac{T_{\text{RH}}}{T_0}, \quad (29)$$

which replaces the naive Planck-scale estimate. Even for $T_{\text{RH}} \sim 10^{15}–10^{16}$ GeV, Eq. (29) yields

$$1 + z_{\text{RH}}^{\text{max}} \sim 10^{27}–10^{29}, \quad (30)$$

several orders of magnitude below the value obtained by extrapolating Eq. (28) to $T \sim T_{\text{Pl}}$. Lower reheating temperatures, required in many inflationary models, reduce $z_{\text{RH}}^{\text{max}}$ further.

If evaporation completes during radiation domination, the mapping is well described by Eq. (28). If, instead, evaporation occurs during a pre-reheating phase—or if PBHs dominate the energy density and their evaporation triggers reheating itself [28, 94]—the relevant redshift is bounded by $z_{\text{RH}}^{\text{max}}$, and the resulting GW spectrum is shifted to higher present-day frequencies. Consequently, the observable peak frequency from PBH evaporation is not determined by the Planck temperature alone, but by the interplay between the microscopic scale $T(M)$ and the macroscopic scale T_{RH} .

C. Modified cosmological histories

The analysis above assumed a standard radiation-dominated background. A wide class of well-motivated early-Universe scenarios predicts nonstandard expansion phases that substantially alter both the frequency and the amplitude of the GW background emitted by evaporating PBHs. We survey three representative cases.

a. Early matter domination. If PBHs are produced in sufficient abundance, their energy density $\rho_{\text{PBH}} \propto a^{-3}$ redshifts more slowly than the radiation bath ($\rho_r \propto a^{-4}$), and the Universe inevitably enters an effectively matter-dominated (MD) phase before evaporation completes [28, 94]. During this phase $a(t) \propto t^{2/3}$ rather than $t^{1/2}$, so the ratio of scale factors between evaporation time t_{ev} and the onset of radiation domination t_{RD} is

$$\frac{a(t_{\text{RD}})}{a(t_{\text{ev}})} = \left(\frac{t_{\text{RD}}}{t_{\text{ev}}} \right)^{2/3}, \quad (31)$$

compared with $(t_{\text{RD}}/t_{\text{ev}})^{1/2}$ in a radiation-dominated background. Because $t_{\text{RD}}/t_{\text{ev}} > 1$, the matter-dominated expansion is *slower*, so gravitons retain a larger comoving frequency—they are *less* redshifted than in the standard case. The observed spectral peak shifts to *higher* present-day frequencies by a factor [95, 96]

$$\frac{f_0^{\text{MD}}}{f_0^{\text{RD}}} \simeq \left(\frac{t_{\text{RD}}}{t_{\text{ev}}} \right)^{1/6}, \quad (32)$$

which can be large for a prolonged MD era, potentially shifting a signal from the MHz band into the GHz band or beyond. An identical enhancement arises whenever a long-lived massive field—a modulus or heavy inflaton condensate—dominates the energy budget prior to decaying into radiation [97, 98].

In addition to shifting the peak, an early MD era imprints a characteristic spectral tilt. Modes that exit the Hubble radius during matter domination and re-enter during radiation domination acquire a transfer-function suppression $\propto f^{-2}$ relative to modes that are always sub-Hubble, generating a spectral break at the frequency corresponding to the Hubble scale at reheating [95, 96]. This break provides an independent observational handle on T_{RH} that does not rely on the black-hole physics setting the peak frequency.

b. Kination. In kination-dominated cosmologies the energy budget is dominated by the kinetic energy of a scalar field, giving equation-of-state parameter $w = 1$ [98–100]. The scale factor grows as $a(t) \propto t^{1/3}$ and the kination energy density redshifts as $\rho_\phi \propto a^{-6}$ —steeper than radiation—so the Universe transitions to radiation domination once the subdominant radiation bath catches up. If PBH evaporation occurs during the kination era, the scale-factor ratio between emission and the kination-to-radiation transition at a_{KR} is

$$\frac{a_{\text{KR}}}{a(t_{\text{em}})} = \left(\frac{t_{\text{KR}}}{t_{\text{em}}} \right)^{1/3}, \quad (33)$$

which is *smaller* than the corresponding radiation-domination factor $(t_{\text{KR}}/t_{\text{em}})^{1/2}$ for equal time intervals. Emitted gravitons are therefore *more* redshifted than in the standard case, shifting the spectral peak to *lower* present-day frequencies—the opposite of early matter domination. The magnitude of the shift depends on the duration of the kination era and can range from a

modest correction to a displacement of several frequency decades [101, 102].

Beyond the peak shift, kination enhances the GW energy density at high frequencies: modes above the kination-to-radiation transition frequency receive a relative boost $\propto f_0^2$ compared with the radiation-dominated prediction [103, 104], generating a blue tilt that can raise Ω_{GW} by many orders of magnitude and potentially bring otherwise undetectable signals within reach of resonant-cavity detectors.

c. Nonstandard reheating temperature. Even within the standard paradigm of radiation domination after inflation, T_{RH} is a free parameter bounded from below by Big Bang Nucleosynthesis [105], $T_{\text{RH}} \gtrsim 4 \text{ MeV}$. As Eq. (29) makes explicit, T_{RH} sets the maximum meaningful redshift for GW emission at or before reheating: reducing T_{RH} lowers $z_{\text{RH}}^{\text{max}}$ and shifts the observed spectrum to higher frequencies for a fixed emission scale. This creates a partial degeneracy—a signal at frequency f_0 could arise from a black hole with the standard Hawking temperature at low T_{RH} , or from a modified-temperature model at high T_{RH} . Breaking the degeneracy requires either an independent constraint on T_{RH} —for example, from the GW background produced during preheating [106, 107] or from the abundance of thermally produced dark matter—or a spectral-shape measurement precise enough to distinguish the two scenarios morphologically.

Entropy injection *after* GW emission—from the decay of a modulus field or a first-order phase transition—dilutes the GW energy density as

$$\Omega_{\text{GW}} \rightarrow \Omega_{\text{GW}} \times \left(\frac{s_{\text{before}}}{s_{\text{after}}} \right)^2 \quad (34)$$

[108], potentially suppressing an otherwise detectable signal below any foreseeable sensitivity threshold. In the absence of such post-emission entropy production the ΔN_{eff} normalization adopted throughout this work remains the primary upper bound on the signal amplitude.

D. Impact on the present-day GW spectrum and detectability

The nonstandard expansion phases discussed above affect the present-day GW spectrum through two largely independent channels: a universal rescaling of the peak frequency and a modification of the spectral shape and amplitude.

a. Frequency rescaling. The dominant effect of any nonstandard epoch is to shift every spectral feature by a common multiplicative factor. The present-day peak frequency can be written schematically as

$$f_0^{\text{peak}} \simeq \frac{T(M_0)}{2\pi} \times \mathcal{R}(w, t_{\text{ev}}, t_{\text{RD}}) \times \frac{a_{\text{ev}}}{a_0} \Big|_{\text{RD}}, \quad (35)$$

where the last factor is the standard radiation-dominated redshift and \mathcal{R} is a dimensionless correction satisfying

$\mathcal{R} > 1$ for $w < 1/3$ (matter domination) and $\mathcal{R} < 1$ for $w > 1/3$ (kination domination throughout the emission epoch). The value of \mathcal{R} can span many orders of magnitude and is degenerate with the model-specific temperature parameter θ in the absence of supplementary information. This is a fundamental limitation of using f_0^{peak} alone as a diagnostic: the same frequency can be produced by arbitrarily many combinations of $(\theta, T_{\text{RH}}, w)$.

b. Spectral shape as a discriminant. The frequency-peak degeneracy is partially broken by the spectral shape. Different expansion histories imprint characteristic tilts and breaks on $\Omega_{\text{GW}}(f_0)$ that are independent of the peak position:

- An early matter-dominated era produces a $\Omega_{\text{GW}} \propto f_0^{-2}$ suppression below the reheating-scale frequency, creating a low-frequency spectral break [95].
- A kination era generates a blue tilt $\Omega_{\text{GW}} \propto f_0^{+2}$ above the kination-to-radiation transition frequency [103], absent in standard cosmology.
- Post-emission entropy dilution suppresses the amplitude uniformly across all frequencies without introducing any spectral distortion, making it degenerate with a reduction in the initial PBH abundance.

These features are in principle observable when the signal-to-noise ratio is sufficient to measure the spectral slope over at least one decade in frequency. Future broadband ground-based interferometers (covering 1–10⁴ Hz) and resonant-cavity arrays in the GHz band could jointly constrain the spectral tilt and thereby discriminate between cosmological and black-hole-physics origins of any observed feature.

c. Amplitude and the ΔN_{eff} constraint. Throughout this work GW spectra are normalized to saturate the ΔN_{eff} bound. If the nonstandard phase ends well before BBN, the constraint is unchanged: $\Delta N_{\text{eff}} \leq 0.3$ limits the total integrated GW energy density at nucleosynthesis [109]. If entropy injection occurs between GW emission and BBN, the effective ΔN_{eff} contribution is diluted accordingly and the normalization falls below the bound adopted here. Conversely, if PBH evaporation itself drives reheating, the GW background and the thermal bath are produced simultaneously; the normalization is then set self-consistently by the initial PBH abundance, and the peak amplitude can significantly exceed our fiducial normalization without tension with N_{eff} [62, 110].

d. Implications for search strategies. These considerations lead to a concrete observational prescription. First, searches should scan a wide frequency range—conservatively $\sim 1 \text{ Hz}$ to $\sim 10^{12} \text{ Hz}$ —rather than targeting only the frequency predicted by the standard Hawking law at a fixed M_0 , because f_0^{peak} is sensitive to both the black-hole and the cosmological physics. Second, spectral-shape measurements carry more diagnostic power than peak-frequency measurements alone: tilts and breaks identify the equation-of-state parameter w during any nonstandard era, after which the peak position constrains

$T(M_0)$ or M_0 for known w . Third, combining a GW detection with an independent constraint on T_{RH} —from, e.g., the thermally produced dark-matter abundance or primordial nucleosynthesis—would significantly tighten the inference on the microscopic temperature model. Finally, in scenarios where PBH evaporation drives reheating, the GW background is accompanied by complementary signatures—dark-matter production, baryon-asymmetry generation, and CMB spectral distortions—that together could break the remaining degeneracies and enable a coherent reconstruction of both the expansion history and the quantum-gravitational physics operative near the Planck scale.

VI. COMPARISON OF MODELS AND RESULTS

With the theoretical framework established in the preceding sections—the modified temperature–mass relations $T(M)$ in Sec. III, the gravitational-wave emission formalism in Sec. IV, and the cosmological redshifting and expansion history in Sec. V—we are now in a position to compute and compare the present-day stochastic GW spectra predicted by each scenario. The goal of this section is threefold: to characterize the spectral morphology produced by each modified-temperature model as a function of its defining parameter, to identify which regions of parameter space yield signals accessible to planned or proposed detectors, and to delineate the physically meaningful parameter range from limiting cases in which the modified model reduces to, or becomes indistinguishable from, the standard Hawking result.

A. Numerical treatment

The GW spectrum is computed by numerically integrating the black-hole mass evolution equation from an initial mass M_0 down to a model-dependent stopping mass M_{stop} , which is either set by the physical domain of $T(M)$ —as in the LQG, non-commutative, and tunneling models—or by a small fraction of M_0 when no such cutoff exists. At each mass step the instantaneous blackbody emission spectrum is evaluated and weighted by the corresponding time interval and scale factor, following the prescription described in Sec. IV. The resulting spectrum is then redshifted to the present day using the formalism of Sec. V and normalized so that the integrated GW energy density saturates the $\Delta N_{\text{eff}} \leq 0.3$ bound from BBN and CMB observations [111, 112]. This normalization provides a physically motivated and model-independent amplitude reference: it corresponds to the maximum signal consistent with current cosmological constraints and therefore represents an optimistic but conservative upper envelope for each model.

Several numerical safeguards are implemented to ensure robustness across the full parameter space. When $T(M)$ vanishes at a finite mass—as in the LQG and NC models—

the integration is halted at $M_{\text{stop}} = (1 + \epsilon)M_{\text{min}}$ to avoid the divergent time step that would arise from a vanishing evaporation rate; we have verified that the spectral shape and normalization are insensitive to the precise value of ϵ for $\epsilon \lesssim 10^{-6}$. For models where $T(M_0) = 0$ identically—which occurs for the tunneling model whenever $M_0 < \sqrt{\gamma}$ —no evaporation takes place and the spectrum is identically zero; such parameter combinations are excluded from the figures presented below. In all cases the frequency grid spans $f_0 = 1\text{--}3 \times 10^{12}$ Hz on a logarithmic mesh of $N = 1400$ points, sufficient to resolve the spectral peak and both asymptotic tails for all models and parameter values considered.

B. Spectral morphologies and parameter dependence

The principal results of our numerical analysis are summarized in Figs. 4 and 5. Figure 4 presents a systematic comparison of all six modified-temperature models at fixed initial mass $M_0 = 10 M_{\text{Pl}}$, with three representative values of each model’s defining parameter chosen to span from the near-standard regime through to the most extreme physically motivated case. Figure 5 then isolates the role of the initial mass by comparing the six models—each evaluated at a single, maximally distinct parameter value—at $M_0 = 10 M_{\text{Pl}}$ and $M_0 = 300 M_{\text{Pl}}$ side by side. In both figures the standard Hawking result is shown as a solid black curve for reference, and the approximate sensitivity envelopes of the Einstein Telescope (ET) [113], Cosmic Explorer (CE) [114], and two resonant-cavity configurations are overlaid to provide a direct assessment of detectability. The BBN/ N_{eff} constraint band is also shown, since it sets the normalization of every curve in the figure.

Before turning to the individual models it is useful to identify the general trends that cut across all six scenarios. Any modification to $T(M)$ that suppresses the temperature relative to the standard Hawking value $T_{\text{H}} = (8\pi M)^{-1}$ slows evaporation, extends the black-hole lifetime, and thereby shifts the emission to earlier times and lower instantaneous frequencies; after cosmological redshifting, this translates directly into a *lower observed peak frequency* f_0^{peak} . The magnitude of the shift scales with the degree of temperature suppression integrated over the evaporation history and can range from a fraction of a decade to more than ten decades in frequency, as the figures make clear. Conversely, any modification that introduces a hard cutoff—either a minimum mass below which evaporation ceases, or a temperature that vanishes at finite M —concentrates the emission into a finite time window, producing a *sharper spectral peak and a steeper high-frequency cutoff* than the standard Hawking spectrum. Models that combine both effects (e.g. a temperature that is suppressed throughout but vanishes at M_{min}) exhibit the most dramatic departures from the standard case, both in peak position and in spectral shape.

A second general observation concerns the role of the normalization. Because all spectra are scaled to the same ΔN_{eff} ceiling, models that deposit their radiation over a narrower frequency range necessarily have higher peak amplitudes. This is not a fine-tuning: it reflects the physical fact that a more monochromatic source must be brighter at its peak in order to carry the same total energy. As a result, the models that are most shifted from the standard Hawking position tend also to have the highest peak $\Omega_{\text{GW}} h^2$, making them simultaneously the most spectrally distinctive and the most amenable to detection by a narrowband instrument. The tension between peak amplitude and integrated energy is encoded in the N_{eff} band shown in the figures, and any confirmed detection at or near this level would immediately imply that Planck-scale black holes contribute a cosmologically significant fraction of the total relativistic energy density at the time of BBN.

With these general trends in mind we now discuss each model in turn.

Fig. 4 displays the predicted gravitational wave energy density $\Omega_{\text{GW}}(f_0) h^2$ for each of the six modified Hawking temperature models considered in this work, computed at initial mass $M_0 = 10 M_{\text{Pl}}$ and normalized so that the integrated signal saturates the current BBN/ N_{eff} bound, $\Delta N_{\text{eff}} \leq 0.3$. The standard Hawking result (black solid curve) serves as the baseline in every panel: its spectrum peaks near $f_0 \sim 10^{10}$ – 10^{11} Hz and falls off steeply on either side, reflecting the near-thermal blackbody emission integrated over the full evaporation history of the black hole. All modified models shift this peak to lower frequencies and, in several cases, alter the spectral shape qualitatively; the magnitude and character of these shifts encode information about the microscopic physics operative near the Planck scale.

Plateau model.—In this scenario the temperature saturates at a finite value $T_{\text{plateau}} \simeq A/M_c$ rather than rising without bound as $M \rightarrow 0$, slowing the final stages of evaporation considerably. As M_c increases from 3 to 3×10^6 (in Planck units) the spectral peak migrates from near the standard Hawking position all the way down to $f_0 \sim 10^2$ – 10^3 Hz, squarely within the design band of next-generation ground-based interferometers such as the Einstein Telescope and Cosmic Explorer. The spectral shape also broadens noticeably at large M_c , a direct consequence of the extended low-temperature epoch during which the black hole lingers before completing its evaporation.

Cooling model.—Here the temperature reaches a maximum at $M = M_c/\sqrt{2}$ before turning over and decreasing back toward zero, so that the black hole effectively stalls and re-heats in a two-stage process. This non-monotonic evolution produces a characteristic double-peaked or strongly asymmetric spectral profile that is qualitatively distinct from all other models considered. For $M_c = 5$ the spectrum is nearly indistinguishable from standard Hawking, but at $M_c = 3000$ the peak has shifted by roughly six decades in frequency, with significant power

deposited at intermediate frequencies $f_0 \sim 10^4$ – 10^6 Hz that would otherwise be inaccessible to any planned detector.

LQG/Planck-star model.—The loop-quantum-gravity inspired temperature vanishes as $M \rightarrow M_{\text{min}}$ from above, enforcing a minimum-mass remnant and halting evaporation before the classical singularity is reached. The spectral peak location is relatively insensitive to M_{min} when $M_{\text{min}} \ll M_0$, shifting by only a few decades as M_{min} runs from 0.3 to 9.9; however, the low-frequency tail is progressively suppressed as $M_{\text{min}} \rightarrow M_0$, because less of the total mass is available to radiate. The overall normalization constraint then forces the peak amplitude upward, keeping the signal in tension with the N_{eff} bound even as its frequency decreases.

Non-commutative geometry model.—This model shares the minimum-mass structure of the LQG case but imposes a stronger suppression, $T_{\text{NC}} \propto (A/M)[1 - (M_{\text{min}}/M)^2]$, which causes the temperature to vanish quadratically rather than as a square root near M_{min} . The resulting spectra are consequently narrower and more sharply peaked than their LQG counterparts at comparable M_{min} . For $M_{\text{min}} = 9.99$ —only marginally below $M_0 = 10$ —the radiating mass window is extremely narrow, and the spectrum becomes highly concentrated around a single characteristic frequency, potentially offering a distinctive monochromatic-like signature.

Tunneling corrections model.—In this scenario perturbative corrections to the emission rate introduce a factor $[1 - \gamma/M^2]$ that suppresses radiation below a mass threshold $M_{\text{stop}} = \sqrt{\gamma}$, mimicking a remnant without imposing a strict cutoff. The spectra shift steeply with γ : increasing γ from 3 to 99 moves the peak by roughly four decades in frequency. Because the suppression factor cuts off emission rather abruptly, the high-frequency side of the spectral peak is steeper than in the Plateau or Cooling cases, making the tunneling model in principle distinguishable from those scenarios if the peak frequency can be measured with sufficient precision.

Hagedorn/string-inspired model.—At high temperatures this model enforces a Hagedorn ceiling $T \leq T_H = A/M_H$, above which the density of string states grows exponentially and absorbs any additional energy. For $M_H \ll M_0$ the Hagedorn temperature is reached early in the evaporation and the spectrum resembles that of a blackbody at constant temperature T_H , yielding a broader, flatter profile. Conversely, for $M_H = 10^8 \gg M_0$ the temperature never approaches T_H during the evaporation, and the spectrum approaches the standard Hawking shape. The intermediate case $M_H = 10^4$ produces the most distinctive spectral distortion, with a pronounced shoulder at intermediate frequencies reflecting the transition between the standard and Hagedorn-limited evaporation regimes.

Taken together, the panels of Fig. 4 illustrate several general lessons. First, any mechanism that slows or halts evaporation near the Planck scale shifts the GW peak to lower frequencies, in some cases by many orders of magnitude, relocating the signal from the MHz–THz band into

the frequency range accessible to future resonant-mass detectors or even ground-based interferometers. Second, the spectral *shape*—peak width, asymmetry, and the behavior of the high- and low-frequency tails—carries independent information about the underlying physics that complements the peak frequency alone; models with qualitatively similar peak positions (e.g. LQG and NC at comparable M_{\min}) can still be distinguished by their spectral morphology. Third, the N_{eff} normalization acts as a lever that trades peak height against total integrated power: models that confine radiation to a narrow frequency band necessarily have higher peak amplitudes, which may place them in tension with cosmological bounds or, conversely, make them more amenable to detection by a narrowband instrument. Finally, the resonant-cavity sensitivity curves underscore that the high-frequency ($\gtrsim 10^6$ Hz) window opened by modified evaporation models is not experimentally unreachable: with sufficiently optimistic but physically motivated cavity parameters, several of the model spectra computed here overlap with projected sensitivities, providing a concrete target for next-generation high-frequency gravitational wave searches.

Fig. 5 compares the gravitational wave spectra of the same six modified-temperature models at two initial black hole masses, $M_0 = 10 M_{\text{Pl}}$ (top panel) and $M_0 = 300 M_{\text{Pl}}$ (bottom panel), with all other parameters held fixed at the values discussed in connection with Fig. 4. The juxtaposition isolates the role of M_0 as a global frequency dial: since the characteristic emission frequency redshifts inversely with the evaporation timescale, which itself scales as M_0^3 in the standard case, increasing M_0 by a factor of thirty displaces every spectral feature toward lower frequencies by roughly $\sim M_0^3 \propto 2.7 \times 10^4$ in the standard Hawking limit, though the precise shift is model-dependent whenever the modified dynamics introduce their own mass scale. This interplay between M_0 and the internal model parameters is the central theme of the figure.

Overall frequency shift with M_0 .—The most immediately striking feature of Fig. 5 is the wholesale migration of all spectral peaks toward lower frequencies as M_0 increases from 10 to $300 M_{\text{Pl}}$. For the standard Hawking curve the peak moves from $f_0 \sim 10^{10}$ Hz down to $f_0 \sim 10^{11}$ Hz at $M_0 = 300$ —somewhat counterintuitively shifted *upward* here because the longer-lived, more massive black hole radiates at lower instantaneous temperature for most of its lifetime, but the precise cosmological redshifting and scale-factor weighting in our toy model shift the observed peak in a non-trivial way. More importantly, the models whose peaks already lay at low frequencies for $M_0 = 10$ (Plateau, Cooling, Tunneling) shift further into the sub-MHz regime at $M_0 = 300$, while the models whose peaks were close to the standard Hawking position (LQG, NC at small M_{\min}) open up a much larger separation from the baseline, making them more easily distinguishable in the larger- M_0 panel.

Relative displacement between models.—A key observation is that the *separation* between the standard Hawking peak and those of the modified models is not merely

rescaled by the same factor as M_0 increases. Models whose characteristic mass scale (M_c , M_{\min} , $\sqrt{\gamma}$, or M_H) is small compared to M_0 are, in a sense, already in their asymptotic regime at $M_0 = 10$, so the additional factor of thirty in M_0 shifts their peaks by roughly the same multiplicative factor as the standard Hawking peak. By contrast, models whose characteristic scale is a significant fraction of M_0 —such as NC with $M_{\min} = 9.99$ or Tunneling with $\gamma = 99$, implying $M_{\text{stop}} \approx 9.95$ —are in a qualitatively different dynamical regime at $M_0 = 300$, where the black hole now has ample mass to radiate well above the threshold before the modified dynamics become operative. This is visible in the bottom panel: the NC and Tunneling curves at $M_0 = 300$ exhibit a more pronounced standard-Hawking-like shoulder on their high-frequency sides, reflecting the early, unmodified phase of evaporation, followed by a sharper cutoff as $M \rightarrow M_{\text{stop}}$.

Implications for detectability.—From a detection standpoint the two panels together map out a two-dimensional parameter space— (M_0, θ) where θ collectively denotes the model-specific parameter—within which different experiments are sensitive. At $M_0 = 10 M_{\text{Pl}}$ the Plateau and Cooling models with large parameter values produce peaks in the 10^2 – 10^4 Hz band, overlapping with the Einstein Telescope and Cosmic Explorer sensitivity curves shown in the figure. Increasing to $M_0 = 300 M_{\text{Pl}}$ pushes those same models further below 10^2 Hz, out of the ground-based band entirely, while simultaneously bringing the LQG and NC peaks—which at $M_0 = 10$ sat near 10^8 – 10^9 Hz and thus required resonant-cavity technology—down into a regime where optimistic cavity sensitivities at $\nu_{\text{ref}} = 1$ GHz may be sufficient. The Hagedorn model at $M_H = 10^8$ is largely unaffected by the change in M_0 because $M_H \gg M_0$ in both cases, and its spectrum remains nearly indistinguishable from standard Hawking; any detection strategy targeting Hagedorn physics therefore requires either a much smaller M_H or an independent handle on M_0 from cosmological considerations.

Spectral shape as a discriminant.—Beyond peak frequency, the spectral *morphology* evolves with M_0 in model-specific ways that provide additional discriminating power. The Cooling model develops an increasingly pronounced low-frequency plateau as M_0 grows, because the longer evaporation allows more time for emission during the slow, declining phase of the temperature; this plateau is largely absent at $M_0 = 10$ but clearly visible at $M_0 = 300$. The Tunneling model, conversely, develops a sharper high-frequency cutoff at larger M_0 , as argued above. The LQG and NC spectra narrow relative to the standard Hawking width as M_{\min}/M_0 decreases, consistent with the expectation that a remnant whose mass is a small fraction of M_0 perturbs only the very end of the evaporation and therefore affects only a narrow range of emission frequencies. These morphological trends suggest that, in a scenario where both the peak frequency and the spectral width can be measured—for instance by a broadband resonant detector or a stochastic background search with multiple frequency bins—simultaneous constraints on M_0 and the

model parameter θ may be achievable without degeneracy.

In summary, Fig. 5 demonstrates that the initial black hole mass M_0 acts not merely as an overall rescaling of the frequency axis but as a parameter that can qualitatively change the relationship between the standard Hawking spectrum and those of modified models. Searches targeting the GW background from Planck-scale black holes should therefore scan both the model-specific parameter space and a range of initial masses, and broadband sensitivity across many decades of frequency—from sub-Hz to THz—will ultimately be required to cover the full landscape of well-motivated quantum-gravity scenarios.

C. Cosmological redshift prescriptions and reheating dilution: the Plateau model as a case study

Figure 6 isolates a question that is logically distinct from the comparison of quantum-gravity models carried out in Fig. 4: given a fixed modified temperature–mass relation, how sensitive is the *observed* gravitational-wave spectrum to the cosmological redshift history between evaporation and today? We answer this question using the Plateau model at $M_c = 30$ as a concrete example, presenting results for two initial masses, $M_0 = 10 M_{\text{Pl}}$ (left panel) and $M_0 = 1000 M_{\text{Pl}}$ (right panel). For each mass we show three redshift prescriptions, applied identically to both the standard Hawking spectrum (black curves) and the Plateau spectrum (orange curves), so that the *relative* displacement between the two always encodes quantum-gravity physics while the *absolute* position of either spectrum reflects the cosmological history.

a. The three redshift prescriptions. The present-day frequency of a graviton emitted at cosmic time t_{em} is $f_0 = f_{\text{em}} a(t_{\text{em}})/a_0$, where the scale factor ratio encodes all of the intervening expansion. We compare three physically motivated choices for the emission epoch.

Prescription 1 (solid curves): the most extreme formal benchmark, in which the standard radiation-domination relation $1 + z \simeq (g_{*S}(T)/g_{*S,0})^{1/3} T/T_0$ is extrapolated all the way to $T = T_{\text{Pl}} \approx 1.22 \times 10^{19}$ GeV. This gives the largest redshift factor, $1 + z_1 \sim 10^{31}$, and therefore places the spectral peak at the *lowest* observed frequency. As discussed in Sec. ??, this extrapolation implicitly assumes radiation domination persists to the Planck epoch, an assumption that fails in any realistic inflationary model; it should therefore be regarded as an absolute lower bound on f_0^{peak} rather than a physical prediction.

Prescription 2 (dashed curves): the scale factor is evaluated at the maximum reheating temperature consistent with the evaporation timescale. Specifically, if the PBH population dominates the energy density prior to evaporation—the large- β regime in which $\Omega_{\text{PBH}} \rightarrow 1$ —then complete evaporation triggers an instantaneous reheating at temperature

$$T_{\text{RH}}(t_{\text{ev}}) \simeq \left(\frac{90}{8\pi^3 g_*} \right)^{1/4} \sqrt{\frac{M_{\text{Pl}}}{t_{\text{ev}}}}, \quad (36)$$

which is substantially lower than T_{Pl} and yields a correspondingly *higher* present-day peak frequency. The associated redshift is $1 + z_2 \sim 10^{27} - 10^{29}$ for the masses shown, several orders of magnitude below $1 + z_1$. However, the PBH-domination scenario also entails a matter-dominated expansion phase between PBH formation at time t_{form} and evaporation at t_{ev} . Because the PBH energy density $\rho_{\text{PBH}} \propto a^{-3}$ redshifts more slowly than radiation ($\rho_r \propto a^{-4}$), gravitons emitted during this phase experience an additional suppression of their energy fraction relative to the post-reheating radiation bath. In the large- β limit this reheating dilution factor takes the form

$$\mathcal{D}_{\text{RH}} \equiv \left(\frac{a_{\text{ev}}}{a_{\text{form}}} \right)^{-1} = \left(\frac{t_{\text{form}}}{t_{\text{ev}}} \right)^{2/3}, \quad (37)$$

where $a \propto t^{2/3}$ during the matter-dominated epoch and $t_{\text{form}} \sim GM_{\text{BH}}/(\gamma c^3)$ is the horizon-crossing formation time with $\gamma = 0.2$. For $M_0 = 10 M_{\text{Pl}}$ the evaporation time is $t_{\text{ev}} \approx 5120\pi M_0^3 t_{\text{Pl}} \approx 8.5 \times 10^{-40}$ s while $t_{\text{form}} \approx 2.7 \times 10^{-42}$ s, giving $a_{\text{ev}}/a_{\text{form}} \approx 46$ and $\mathcal{D}_{\text{RH}} \approx 2 \times 10^{-2}$. For $M_0 = 1000 M_{\text{Pl}}$ the cubic scaling of t_{ev} and linear scaling of t_{form} with M_0 combine to give $a_{\text{ev}}/a_{\text{form}} \approx 2 \times 10^6$ and $\mathcal{D}_{\text{RH}} \approx 5 \times 10^{-7}$, consistent with the dilution factor $\times 10^{-5}$ indicated in the legend of the right panel. This suppression is applied multiplicatively to the $\Omega_{\text{GW}} h^2$ amplitude of *both* the standard Hawking and Plateau curves in Prescription 2, visible as the uniform downward displacement of all dashed curves relative to their solid counterparts at the same peak frequency.

Prescription 3 (dotted curves): the gravitons are redshifted from the background radiation temperature at the evaporation epoch under the assumption that the universe is radiation-dominated throughout,

$$T_{\text{RD}}(t_{\text{ev}}) \simeq \sqrt{0.301} \left(\frac{M_{\text{Pl}}}{t_{\text{ev}}} \right)^{1/2} g_*^{-1/4}, \quad (38)$$

which is parametrically similar to T_{RH} but does not invoke PBH domination. In Prescription 3 no dilution factor is applied: the PBHs are treated as a subdominant component that evaporates into an already-radiation-dominated background. Consequently the dotted curves share the amplitude normalization of Prescription 1 but are shifted to higher frequencies, tracing the same spectral shape as the solid curves displaced rigidly along the frequency axis.

b. Frequency separation and degeneracy structure. The three prescriptions produce peak frequencies that differ by multiple decades, illustrating the fundamental degeneracy noted in Sec. V: the same internal temperature model, at a fixed M_0 , can populate any frequency window from below 10^5 Hz to above 10^{15} Hz depending solely on the assumed cosmological history. Conversely, a measured peak frequency places a joint constraint on $(M_0, T(M), T_{\text{RH}})$ that cannot be broken by the peak position alone.

The relative displacement *between* the standard Hawking and Plateau curves is, however, cosmology-independent: both spectra are shifted by the same

redshift factor under each prescription, so the ratio $f_0^{\text{peak}}(\text{Plateau})/f_0^{\text{peak}}(\text{Std})$ and the spectral-shape difference are intrinsic to the quantum-gravity model. This invariance is the key discriminating feature: a broadband measurement that resolves both peaks—or measures the spectral slope and width on either side of a single peak—can in principle constrain $T(M)$ independently of the cosmological background, provided the *shape* of the signal, rather than its absolute position, is used as the primary observable.

c. Amplitude effects of reheating dilution. In the PBH-domination scenario (Prescription 2), the dilution factor \mathcal{D}_{RH} can reduce $\Omega_{\text{GW}} h^2$ by many orders of magnitude relative to the ΔN_{eff} ceiling. For $M_0 = 1000 M_{\text{Pl}}$ the suppression reaches $\sim 10^{-6}$ – 10^{-7} , bringing the dashed curves well below the $\Delta N_{\text{eff}} = 0.3$ band and potentially below the reach of any proposed resonant detector. This has two important implications. First, the large- β (PBH domination) scenario is self-consistently the *least* favorable for detection, despite placing the spectral peak at frequencies intermediate between Prescriptions 1 and 3: the gain in peak frequency is more than offset by the amplitude suppression. Second, the dilution is stronger for heavier PBHs, because $\mathcal{D}_{\text{RH}} \propto (t_{\text{form}}/t_{\text{ev}})^{2/3} \propto M_0^{(1-3)\times 2/3} = M_0^{-4/3}$; increasing M_0 therefore simultaneously shifts the spectral peak to lower frequencies (via longer t_{ev}) and suppresses the amplitude more severely. Taken together, these trends suggest that the most detectable signals in the PBH-domination regime come from the lightest PBHs, for which the dilution is least severe and the peak frequency may still lie within a detectable band.

d. Comparison of the two panels: role of M_0 . The right panel ($M_0 = 1000 M_{\text{Pl}}$) demonstrates the combined effect of increasing the initial mass by two orders of magnitude. Under Prescriptions 1 and 3 (solid and dotted), where no dilution is applied, all spectral features shift to lower frequencies by a factor of order $M_0^3 \sim 10^9$ relative to the left panel, consistent with the standard Hawking evaporation timescale $\tau_{\text{ev}} \propto M_0^3$. The Plateau model peak, already displaced from the standard Hawking peak in the left panel, shifts even further in the right panel: at $M_0 = 1000 M_{\text{Pl}}$ and Prescription 1, the Plateau peak reaches frequencies below $\sim 10^5$ Hz, below the displayed axis range, while under Prescription 3 it moves into the sub-MHz regime close to the ultra-low-frequency (MHz) resonant-cavity sensitivity band. Under Prescription 2 the dilution factor is so severe ($\mathcal{D}_{\text{RH}} \sim 10^{-6}$) that the dashed curves are suppressed by six decades in amplitude, rendering them undetectable with the instrument concepts considered here.

e. Detectability prospects. The three resonant-cavity sensitivity envelopes shown in Fig. 6—the GHz-scale optimistic concept (10^8 – 3×10^9 Hz), the MHz lumped-element concept (10^6 – 10^8 Hz), and the futuristic UVHF concept (10^{12} – 10^{16} Hz)—each touch at least one of the signal curves in one of the two panels, but only under the most favorable redshift prescription (Prescription 3) and without the reheating dilution penalty. Specifically, for

$M_0 = 10 M_{\text{Pl}}$ under Prescription 3, the Plateau spectrum peaks near 10^{13} – 10^{14} Hz, overlapping with the lower edge of the UVHF concept band. For $M_0 = 1000 M_{\text{Pl}}$ under Prescription 3 the same model produces a peak near 10^6 – 10^7 Hz, squarely within the MHz concept band. These intersections survive the ΔN_{eff} normalization and represent physically realizable—if experimentally challenging—detection targets.

The figure therefore conveys two complementary lessons for experimental strategy. First, searches for PBH evaporation signals must scan a frequency range spanning at least ten decades (conservatively 10^5 – 10^{15} Hz) to cover the full envelope of cosmological uncertainties at any fixed M_0 . Second, spectral-shape measurements are essential for separating quantum-gravity physics from cosmological backgrounds: the relative displacement between the standard Hawking peak and the modified-model peak, and in particular the asymmetry and width of each spectral feature, carry model-specific information that is preserved across all three redshift prescriptions. Broadband sensitivity, or equivalently the ability to measure both the peak frequency and the spectral slope over adjacent decades, therefore provides substantially more diagnostic power than a single narrowband detection.

D. Experimental considerations for resonant detectors

The sensitivity curves shown throughout this work represent scan-averaged envelopes over multi-year observation campaigns rather than instantaneous broadband sensitivities [72], and should be interpreted accordingly. Table I summarises the benchmark assumptions for the three detector concepts; here we briefly comment on the principal challenges facing each.

At GHz frequencies (10^8 – 10^9 Hz), the detection strategy relies on inverse-Gertsenshtein conversion of gravitational-wave strain into photons inside a strong magnetic field [67, 69–71]. The central tension is maintaining ultra-high quality factors ($Q \sim 10^{11}$) in the strong magnetic fields ($B \sim 35$ T) required for efficient conversion, since superconducting resonators are typically quenched by large static fields [115]. Viable architectures must spatially separate the high-field interaction region from the low-loss readout [71], and scale the effective volume to $V \sim 10^2$ – 10^3 m³ through coherent cavity arrays rather than monolithic structures [68, 72]. Quantum-limited amplification [116], and potentially squeezed-state or back-action-evading readout [117], will be necessary to reach the mK-scale noise temperatures assumed here over decade-long scans.

In the MHz band (10^6 – 10^8 Hz), lumped-element LC or magneto-quasistatic sensor architectures are more natural [118], but technical noise sources—microphonics, magnetic pickup, and $1/f$ electronic noise—become the dominant limitation. As at GHz frequencies, achieving large effective inductive volumes in strong fields will require

multiplexed, array-based designs with parallelised readout and coherent combination [72].

The UVHF concept (10^{12} – 10^{16} Hz) is qualitatively more speculative: at optical and infrared frequencies there is currently no established transduction mechanism coupling gravitational-wave strain to a photonic resonant mode with nonnegligible overlap factor η_n [72]. Even setting aside this fundamental challenge, the effective volumes and quality factors ($Q \sim 10^{14}$) assumed in our benchmark would require phase-locked networks of photonic resonators on macroscopic scales [119], well beyond the current state of the art. The UVHF sensitivity curve should therefore be understood as a long-range aspirational target rather than a near-term projection.

Across all regimes, the dominant experimental levers are the effective interaction volume, the noise floor, and the ability to coherently combine multiple resonant elements while maintaining calibration over multi-year scans [72]. The benchmarks in Table I delineate the level of experimental control required to probe the GW backgrounds predicted here, and should motivate a phased programme beginning with proof-of-concept GHz cavities and extending progressively toward the MHz and UVHF bands.

VII. CONCLUSIONS AND OUTLOOK

We have developed a comprehensive framework for using the stochastic gravitational-wave background produced by evaporating primordial black holes as a probe of quantum gravity near the Planck scale. The central thesis of this work—that modifications to the Hawking temperature–mass relation $T(M)$ leave distinctive, potentially observable imprints in the graviton emission spectrum—has been substantiated through a systematic numerical study of six representative classes of beyond-semiclassical physics, spanning plateau/saturation models, cooling scenarios, loop-quantum-gravity and noncommutative-geometry inspired remnant-forming relations, tunneling and backreaction-based corrections, and Hagedorn/string-inspired limiting-temperature models. A central new result of this work is to treat the cosmological redshift history not merely as a nuisance parameter but as an independent diagnostic channel, and to quantify how reheating dilution in the PBH-domination regime modifies both the amplitude and the frequency placement of the signal. We summarize the principal findings, assess the prospects for observational detection, and identify the most promising directions for future work.

A. Summary of main findings

Our results admit a concise organizing principle: *any modification to $T(M)$ that reduces the temperature below the standard Hawking value shifts the GW spectral peak to lower frequencies, while any modification that introduces a hard cutoff sharpens the peak and steepens the high-*

frequency tail. The two effects can operate independently or in combination, and together they span the full range of qualitative behaviors seen in the figures.

More specifically, the main findings of this work are as follows.

Spectral diversity.—The six modified-temperature models studied here produce present-day GW spectra that differ from the standard Hawking result by up to ten or more decades in peak frequency and by order-of-magnitude differences in spectral width and shape. Even models that share the same qualitative behavior—such as the LQG and NC scenarios, both of which predict a minimum mass and a vanishing temperature at M_{\min} —are distinguishable through their spectral morphology, since the NC suppression is quadratic in M_{\min}/M while the LQG suppression is only square-root, leading to measurably different peak widths and asymptotic tails at comparable parameter values.

Parameter sensitivity.—The location of the spectral peak is exquisitely sensitive to the model-defining parameter. In the plateau and cooling models, shifting M_c from a few M_{Pl} to 10^3 – $10^6 M_{\text{Pl}}$ moves the peak by six or more decades, sweeping it from the standard GHz–THz band down into the Hz–kHz range accessible to ground-based interferometers. In the tunneling model, the analogous shift requires only a modest change in γ , with the stopping mass $M_{\text{stop}} = \sqrt{\gamma}$ providing a direct spectral ruler. These sensitivities imply that even a coarse frequency measurement of a GW peak would constrain the model parameter to within a factor of a few.

Role of initial mass.—The initial black-hole mass M_0 acts as a global frequency dial, but its effect is non-trivially entangled with the model-specific scale. For models whose characteristic parameter is small compared to M_0 , increasing M_0 shifts all spectral features by a common factor of order M_0^3 in the standard Hawking limit. For models whose cutoff scale is a significant fraction of M_0 , the qualitative character of the spectrum changes: the black hole spends a larger fraction of its lifetime in the unmodified regime, producing a standard-Hawking-like shoulder on the high-frequency side and a sharp modified cutoff at lower frequencies. Jointly varying M_0 and the model parameter is therefore necessary for a complete survey of the signal landscape.

Cosmological history as an additional dial.—The expansion history between evaporation and today introduces an independent layer of model dependence that is in principle separable from the black-hole physics. An early matter-dominated era reduces the redshift experienced by the emitted gravitons, shifting all spectral features to higher present-day frequencies and imprinting a characteristic $\Omega_{\text{GW}} \propto f_0^{-2}$ break at the reheating scale; kination does the opposite, pushing the spectrum to lower frequencies and generating a blue f_0^{+2} high-frequency tilt. Crucially, these cosmological imprints are *spectral-shape effects*, not merely rescalings of the peak frequency, so a broadband measurement can in principle disentangle them from the black-hole temperature modifications of primary interest.

TABLE I. Summary of resonant–detector benchmark assumptions adopted in this work. Quoted sensitivities are scan–averaged envelopes over the stated frequency ranges rather than instantaneous bandwidths.

	GHz cavity (10^8 – 10^9 Hz)	Low–frequency LC (10^6 – 10^8 Hz)	UVHF resonant concept (10^{12} – 10^{16} Hz)
Reference frequency ν_{ref}	1 GHz	50 MHz	100 THz
Scan range	10^8 – 3×10^9 Hz	10^6 – 10^8 Hz	10^{12} – 10^{16} Hz
Magnetic field B	~ 35 T	~ 35 T	~ 30 T
Effective volume V	$\sim 3 \times 10^2$ m ³	$\sim 3 \times 10^2$ m ³	$\sim 10^8$ m ³ (effective)
Quality factor Q	$\sim 10^{11}$	$\sim 10^{11}$	$\sim 10^{14}$
System noise T_{sys}	~ 5 mK	~ 5 mK	~ 1 mK (equiv.)
Overlap factor η_n	~ 0.5	~ 0.5	~ 0.3
Per–step bandwidth $\Delta\nu$	$\sim 10^6$ Hz	$\sim 5 \times 10^6$ Hz	$\sim 10^{10}$ Hz
Total scan time t	~ 10 yr	~ 10 yr	~ 3 yr
Dominant challenges			
	<ul style="list-style-type: none"> • High Q in strong B • Scaling to large V via arrays • Quantum–limited microwave readout • Long–term scan stability 	<ul style="list-style-type: none"> • Microphonics and $1/f$ noise • Large inductive volumes in strong B • High Q with practical coupling • Parallelised scanning 	<ul style="list-style-type: none"> • No established transduction mechanism • Coherent scaling to large V_{eff} • Ultra–high–Q photonic resonators • Quantum–limited optical readout

Reheating dilution as an amplitude suppressor.—Figure 6 introduces a qualitatively new result not captured by the frequency-shift analysis alone: when PBHs dominate the pre-reheating energy budget (the large- β regime), evaporation triggers an epoch of matter-dominated expansion between formation at $t_{\text{form}} \sim GM/(\gamma c^3)$ and complete evaporation at $t_{\text{ev}} \propto M_0^3 t_{\text{Pl}}$. The graviton energy fraction is diluted by a factor

$$\mathcal{D}_{\text{RH}} = \left(\frac{t_{\text{form}}}{t_{\text{ev}}} \right)^{2/3} \propto M_0^{-4/3}, \quad (39)$$

which suppresses $\Omega_{\text{GW}} h^2$ by several orders of magnitude relative to the ΔN_{eff} ceiling and grows rapidly with M_0 . For $M_0 = 10 M_{\text{Pl}}$ the suppression is modest ($\mathcal{D}_{\text{RH}} \sim 10^{-2}$), but for $M_0 = 1000 M_{\text{Pl}}$ it reaches $\sim 10^{-6}$ – 10^{-7} , rendering the reheating-dominated signal undetectable with any instrument concept considered here. Crucially, the dilution is stronger for heavier PBHs, so the large- β scenario is simultaneously the most interesting cosmologically—it connects PBH evaporation directly to reheating—and the most challenging observationally. The most favorable detection targets within this scenario are therefore the lightest PBHs, $M_0 \sim \mathcal{O}(10) M_{\text{Pl}}$, for which \mathcal{D}_{RH} is least severe and the spectral peak may still lie within a technologically accessible frequency band.

Cosmology-independence of the relative spectral displacement.—A key implication of Fig. 6 is that, while the *absolute* position of the spectral peak depends strongly on the assumed redshift prescription, the *relative* displacement between the standard Hawking peak and the modified-model peak is cosmology-independent: both

spectra are shifted by the same scale-factor ratio under any given prescription. Likewise, the amplitude suppression from reheating dilution applies uniformly to both the standard and modified curves, preserving their ratio. This invariance means that the spectral-shape difference and the ratio of peak frequencies—rather than their individual values—are the cleanest observables for constraining $T(M)$, because they are insensitive to the uncertain expansion history between evaporation and today.

Normalization and N_{eff} as a lever.—Normalizing all spectra to saturate $\Delta N_{\text{eff}} \leq 0.3$ provides a physically motivated and model-independent upper envelope. A corollary of this normalization is that models which confine their emission to a narrow frequency band are necessarily brighter at the peak, making them simultaneously the most spectrally distinctive and the easiest targets for narrowband detectors. A confirmed detection at or near the ΔN_{eff} ceiling would immediately establish that Planck-scale black holes contribute a cosmologically significant fraction of the relativistic energy budget at BBN, a conclusion of profound importance independent of which specific quantum-gravity model is responsible. When reheating dilution is operative, however, the observed amplitude can lie many orders of magnitude below this ceiling; any such detection would then provide a direct measure of \mathcal{D}_{RH} and hence of β , the initial PBH abundance.

B. Limits on the observability of Planck-scale evaporation signatures

Despite the encouraging breadth of the signal landscape, several fundamental and practical limitations constrain the observability of the signatures discussed in this work.

Frequency gap.—The standard Hawking prediction for $M_0 \sim 10\text{--}100 M_{\text{Pl}}$ places the spectral peak in the GHz–THz regime, far above the design bands of current and near-term interferometric detectors. Only modified-temperature models with large characteristic scales—or initial masses well above $100 M_{\text{Pl}}$ —shift the peak into the kHz–MHz range accessible to ET and CE. The sub-kHz window, although in principle reachable for extreme parameter choices, would require either very large M_0 or modifications so dramatic that the signal becomes a marginal perturbation on cosmological scales. Absent a breakthrough in broadband sensitivity above $\sim 10^4$ Hz, the most generic predictions of quantum-gravity-inspired evaporation scenarios will remain inaccessible to ground-based interferometry alone.

Cosmological degeneracies and the three-prescription spread.—As illustrated explicitly in Fig. 6, the same quantum-gravity model at a fixed M_0 can populate any frequency window from $\lesssim 10^5$ Hz to $\gtrsim 10^{15}$ Hz depending on the assumed cosmological history. Extrapolating the radiation-dominated redshift formula to T_{Pl} (Prescription 1) places the peak at the lowest accessible frequencies; evaluating the redshift at $T_{\text{RH,max}}(t_{\text{ev}})$ with the associated matter-domination dilution (Prescription 2) shifts it upward by several decades while simultaneously suppressing the amplitude; and treating the PBHs as a subdominant component evaporating into a radiation-dominated background (Prescription 3) yields the highest peak frequency at undiminished amplitude. These three curves span the plausible envelope of cosmological uncertainty and should be regarded as bounding the expected signal location rather than selecting a unique prediction. Breaking the resulting degeneracy between $T(M)$, M_0 , and the redshift history requires either independent external constraints on T_{RH} —from, e.g., thermally produced dark-matter abundances or CMB spectral distortions—or a spectral-shape measurement precise enough to distinguish the morphological signatures of different expansion histories.

Resonant detector requirements.—The resonant-cavity sensitivity curves overlaid on our figures represent aggressive but not implausible benchmarks, requiring magnetic fields $B \sim 25\text{--}35$ T, quality factors $Q \sim 10^{10}\text{--}10^{11}$, effective volumes $V \sim 10^1\text{--}10^2$ m³, and system noise temperatures $T_{\text{sys}} \sim \text{few} \times 10$ mK sustained over multi-year observation campaigns. The futuristic UVHF concept shown in Fig. 6—with effective volume $V_{\text{eff}} \sim 10^8$ m³, $Q \sim 10^{14}$, and $T_{\text{sys}} \sim 1$ mK—is considerably more demanding and should be understood as a long-range aspirational target rather than a near-term projection. The key technical tensions—maintaining ultra-high Q in strong magnetic fields, scaling to large volumes through cavity arrays,

and achieving quantum-limited readout over decade-long scans—are identified explicitly in Sec. V, and none has been resolved at the required level. The projections presented here should therefore be understood as targets for a new generation of instruments rather than forecasts for existing technology.

Model dependence of the toy framework.—The numerical spectra presented in this work are based on a phenomenological, dimensionless evaporation model that captures the qualitative physics of Hawking radiation but does not include several quantitatively important effects: spin-dependent greybody factors, the full Standard Model particle spectrum and its energy-dependent emission rates, possible angular momentum of the initial PBH population, and the detailed cosmological mass function of PBHs at formation. Incorporating these refinements will shift the spectral peak and alter the shape at the factor-of-a-few level, and a fully quantitative prediction for a specific model will require dedicated microphysical calculations beyond the scope of this work.

C. Future directions

The results presented here motivate several concrete directions for follow-up investigation.

Multi-messenger connections.—The same evaporation event that produces the GW background also generates a spectrum of Standard Model particles. The non-gravitational Hawking products—photons, neutrinos, if produced below the respective thermalization scale, as well as light beyond-Standard-Model states, if they exist—contribute to the diffuse cosmic backgrounds at MeV–GeV energies and to the dark matter abundance if stable Planck-scale remnants form [29, 38]. Jointly analyzing the GW signal and these particle backgrounds would provide correlated constraints on both $T(M)$ and the initial PBH mass function, substantially reducing the degeneracies discussed above. In the PBH-domination scenario specifically, where \mathcal{D}_{RH} suppresses the GW amplitude by a precisely computable factor, the non-gravitational particle yield provides an independent handle on β , thereby breaking the degeneracy between the dilution-suppressed GW amplitude and a genuinely sub-dominant PBH contribution. In scenarios where PBH evaporation drives reheating, additional connections to CMB spectral distortions, baryon asymmetry generation, and the effective number of relativistic species at BBN provide a rich multi-observable program [62, 110].

Quantum gravity phenomenology.—Each of the temperature–mass relations studied here was motivated by a specific quantum-gravity framework, but the connection between the phenomenological parameters (M_c , M_{min} , γ , M_H) and the fundamental constants of those theories (e.g. the GUP deformation parameter β , the LQG polymer scale, the string length) has been left at the level of order-of-magnitude correspondence. A tighter mapping between microphysical parameters and spectral

observables would substantially increase the diagnostic power of a GW detection: for instance, the string length inferred from a Hagedorn-shoulder measurement could be compared directly with constraints from particle phenomenology and collider experiments, providing a genuinely cross-disciplinary test of quantum gravity.

Improved evaporation modeling.—Several physically important effects not included in the present framework warrant dedicated study. The role of black-hole spin is particularly notable: rapidly rotating PBHs emit a substantially larger fraction of their power in gravitons than non-rotating ones, and they spin down through superradiant emission before the final Planckian phase, potentially modifying both the overall GW amplitude and the spectral shape [32]. A systematic study of the Kerr case for each of the temperature models considered here would determine whether spin introduces new spectral features—such as polarization anisotropy or a distinctive high-frequency bump associated with the spindown epoch—that could serve as additional discriminants. Similarly, extending the framework to include a distribution of initial masses (a PBH mass function) rather than a single M_0 would smear the spectral peak and could either wash out or accentuate model-specific features depending on the width of the distribution. The reheating dilution factor \mathcal{D}_{RH} would also acquire a distribution in this case, since $\mathcal{D}_{\text{RH}} \propto M_0^{-4/3}$ depends sensitively on mass; heavier members of the PBH population would contribute negligibly to the GW background in the PBH-domination regime, effectively imposing a light-mass selection on the detectable signal.

Refined treatment of the cosmological redshift history.—The three-prescription comparison shown in Fig. 6 motivates a more systematic treatment of the pre-reheating expansion history as a *simultaneous* target of inference, rather than a source of uncertainty to be marginalized over. A Bayesian framework that jointly samples $(M_0, \theta, T_{\text{RH}}, \beta)$ —where θ denotes the model-specific quantum-gravity parameter—using the spectral shape, peak position, and amplitude as observables could in principle separate these contributions from a single broadband detection. The spectral slopes introduced by early matter domination ($\Omega_{\text{GW}} \propto f_0^{-2}$) and kination ($\Omega_{\text{GW}} \propto f_0^{+2}$), together with the amplitude suppression from reheating dilution, provide enough independent constraints to make such a joint inference tractable if the signal-to-noise ratio is sufficient across multiple frequency decades.

High-frequency detector development.—The most direct implication of this work for experiment is the identification of specific frequency–amplitude targets that quantum-gravity-motivated GW spectra are expected to occupy. The resonant-cavity benchmarks adopted here span the MHz–GHz regime and correspond to modifications with $M_c \sim 10^3\text{--}10^6 M_{\text{Pl}}$, $M_{\text{min}}/M_0 \sim 0.1\text{--}1$, or $\sqrt{\gamma}/M_0 \sim 0.1\text{--}1$ —ranges that are physically well motivated and not already excluded by any existing constraint. Even for Prescription 3 (the most favorable cosmological scenario) the signal touches the sensitivity envelope of the GHz or

MHz cavity concepts only in a narrow region. A phased experimental program, beginning with proof-of-concept GHz cavities and progressively extending to MHz-scale lumped-element arrays and ultimately to UVHF resonant concepts in the THz band, would systematically explore this landscape. Crucially, the spectral-shape information available from a broadband resonant array—as opposed to a single narrowband detector—is essential for both model discrimination and cosmological separation, making the case for investing in frequency-agile or multiplexed detector architectures rather than monolithic single-frequency instruments.

Theoretical completeness.—Finally, this work has treated the modified temperature–mass relations as independent phenomenological inputs, without examining whether they are mutually consistent or whether they can be embedded in a single ultraviolet-complete framework. A more ambitious program would seek a unified description of black-hole thermodynamics that interpolates smoothly between the well-tested semiclassical regime and the quantum-gravitational endpoint, making predictions for all thermodynamic quantities—temperature, entropy, heat capacity, and luminosity—from a single set of first-principles assumptions. The gravitational-wave spectrum, by virtue of its sensitivity to the entire evaporation history rather than just the endpoint, is uniquely suited to constrain such a unified description and thereby discriminate between competing proposals for the ultraviolet completion of gravity.

In summary, high-frequency gravitational waves from the evaporation of near-Planck-mass primordial black holes represent a uniquely motivated and potentially accessible window into quantum gravity. Unlike most proposed probes of Planck-scale physics, the Hawking evaporation process has a well-understood semiclassical limit against which departures can be systematically parameterized, and the gravitational-wave signal it produces is, in principle, calculable within each quantum-gravity framework to the extent that the effective temperature–mass relation is specified. Our analysis also highlights how the cosmological environment at the time of evaporation is not merely a spectator, but an active participant that can shift the spectral peak by many decades and suppress the amplitude by orders of magnitude. Separating the quantum-gravity signal from these cosmological effects—and ultimately exploiting them as a complementary probe of the pre-reheating universe—is both the principal challenge and the principal opportunity of this observational program. The observational challenge is formidable, but the physical stakes—simultaneous empirical access to the quantum structure of spacetime and the thermodynamic history of the early universe—justify the ambition. We hope that the framework developed here will serve as a useful foundation for both theoretical refinements and experimental planning as the high-frequency gravitational-wave frontier opens in the coming decades.

Appendix A: Temperature–mass relations used in the toy study

Note that everything is in dimensionless units, with masses in units of M_{Pl} , $A = 1/(8\pi)$.

$$T_{\text{std}}(M) = \frac{A}{M}. \quad (\text{A1})$$

$$T_{\text{plat}}(M) = \frac{A}{\sqrt{M^2 + M_c^2}}, \quad (M_c > 0). \quad (\text{A2})$$

$$T_{\text{cool}}(M) = A \frac{M}{M^2 + M_c^2}, \quad (M_c > 0). \quad (\text{A3})$$

$$T_{\text{GUP}}(M) = A \frac{2M}{\beta} \left[1 - \sqrt{1 - \frac{\beta}{M^2}} \right], \quad M \geq \sqrt{\beta}, \quad (\text{A4})$$

where $\beta > 0$ is the deformation parameter (and the square-root enforces a minimal mass scale).

$$T_{\text{LQG}}(M) = \frac{A}{M} \sqrt{1 - \left(\frac{M_{\text{min}}}{M} \right)^2}, \quad M \geq M_{\text{min}}. \quad (\text{A5})$$

$$T_{\text{NC}}(M) = \frac{A}{M} \left[1 - \left(\frac{M_{\text{min}}}{M} \right)^2 \right], \quad M \geq M_{\text{min}}. \quad (\text{A6})$$

$$T_{\text{tun}}(M) = \frac{A}{M} \left(1 - \frac{\gamma}{M^2} \right), \quad M \geq \sqrt{\gamma}, \quad (\text{A7})$$

with $\gamma > 0$.

$$T_{\text{Hag}}(M) = \frac{T_H}{1 + \left(\frac{M}{M_H} \right)^p}, \quad T_H \equiv \frac{A}{M_H}, \quad (\text{A8})$$

so that for $p = 1$ one has $T_{\text{Hag}}(M) \rightarrow A/M$ at $M \gg M_H$, while for $M \ll M_H$ the temperature saturates to T_H .

-
- [1] S. Carlip, Rept. Prog. Phys. **64**, 885 (2001), arXiv:gr-qc/0108040.
- [2] C. Kiefer, *Quantum Gravity*, 3rd ed., International Series of Monographs on Physics, Vol. 155 (Oxford University Press, 2012).
- [3] S. W. Hawking, Nature **248**, 30 (1974).
- [4] S. W. Hawking, Commun. Math. Phys. **43**, 199 (1975).
- [5] J. M. Bardeen, B. Carter, and S. W. Hawking, Commun. Math. Phys. **31**, 161 (1973).
- [6] J. D. Bekenstein, Phys. Rev. D **7**, 2333 (1973).
- [7] G. Amelino-Camelia, J. R. Ellis, N. E. Mavromatos, D. V. Nanopoulos, and S. Sarkar, Nature **393**, 763 (1998), arXiv:astro-ph/9712103.
- [8] Z. Xiao and B.-Q. Ma, Phys. Rev. D **80**, 116005 (2009), arXiv:0909.4927 [hep-ph].
- [9] MAGIC Collaboration, Phys. Rev. Lett. **125**, 021301 (2020), arXiv:2001.09728.
- [10] H.E.S.S. Collaboration, Astropart. Phys. **34**, 738 (2011), arXiv:1101.3650.
- [11] G. Amelino-Camelia, Phys. Rev. D **62**, 024015 (2000), arXiv:gr-qc/9903080.
- [12] Y. J. Ng and E. S. Perlman, Universe **8**, 382 (2022), arXiv:2205.12852 [gr-qc].
- [13] E. Steinbring, Astrophys. J. **655**, 714 (2007), arXiv:astro-ph/0610422.
- [14] E. S. Perlman *et al.*, Astrophys. J. **805**, 10 (2015), arXiv:1411.7262.
- [15] L. P. Grishchuk, Sov. Phys. JETP **40**, 409 (1975).
- [16] A. A. Starobinsky, JETP Lett. **30**, 682 (1979).
- [17] M. Bojowald, Phys. Rev. Lett. **86**, 5227 (2001), arXiv:gr-qc/0102069.
- [18] A. Ashtekar, A. Corichi, and P. Singh, Phys. Rev. D **77**, 024046 (2008), arXiv:0710.3565.
- [19] K. Abazajian *et al.* (CMB-S4), Astrophys. J. **926**, 54 (2022), arXiv:2008.12619 [astro-ph.CO].
- [20] M. Maggiore, Phys. Lett. B **304**, 65 (1993), arXiv:hep-th/9301067.
- [21] F. Scardigli, Phys. Lett. B **452**, 39 (1999).
- [22] I. Pikovski, M. R. Vanner, M. Aspelmeyer, M. S. Kim, and v. Brukner, Nature Phys. **8**, 393 (2012), arXiv:1111.1979.
- [23] J. E. McClintock *et al.*, Class. Quant. Grav. **28**, 114009 (2011), arXiv:1101.0811.
- [24] Event Horizon Telescope Collaboration, Astrophys. J. Lett. **875**, L1 (2019), arXiv:1906.11238.
- [25] Event Horizon Telescope Collaboration, Astrophys. J. Lett. **930**, L12 (2022), arXiv:2311.08680.
- [26] R. Carballo-Rubio, F. Di Filippo, S. Liberati, and M. Visser, JCAP **08**, 055, arXiv:2205.13555.
- [27] B. J. Carr and S. W. Hawking, Mon. Not. Roy. Astron. Soc. **168**, 399 (1974).
- [28] B. J. Carr, K. Kohri, Y. Sendouda, and J. Yokoyama, Phys. Rev. D **81**, 104019 (2010), arXiv:0912.5297 [astro-ph.CO].
- [29] B. Carr, K. Kohri, Y. Sendouda, and J. Yokoyama, Rept. Prog. Phys. **84**, 116902 (2021), arXiv:2002.12778 [astro-ph.CO].
- [30] R. M. Wald, *Quantum Field Theory in Curved Spacetime and Black Hole Thermodynamics* (University of Chicago Press, 1994).
- [31] N. D. Birrell and P. C. W. Davies, *Quantum Fields in Curved Space*, Cambridge Monographs on Mathematical Physics (Cambridge University Press, 1984).
- [32] D. N. Page, Phys. Rev. D **13**, 198 (1976).
- [33] S. B. Giddings, Phys. Rev. D **46**, 1347 (1992), arXiv:hep-th/9203059.

- [34] S. D. Mathur, *Class. Quant. Grav.* **26**, 224001 (2009), arXiv:0909.1038 [hep-th].
- [35] A. R. Brown, L. V. Iliesiu, G. Penington, and M. Usatyuk, *JHEP* **01**, 109, arXiv:2411.03447 [hep-th].
- [36] G. Lin, L. V. Iliesiu, and M. Usatyuk, *JHEP* **08**, 220, arXiv:2504.21077 [hep-th].
- [37] Y. Aharonov, A. Casher, and S. Nussinov, *Phys. Lett. B* **191**, 51 (1987).
- [38] P. Chen, Y. C. Ong, and D.-h. Yeom, *Phys. Rept.* **603**, 1 (2015), arXiv:1412.8366.
- [39] D. N. Page, *Phys. Rev. Lett.* **71**, 3743 (1993), arXiv:hep-th/9306083.
- [40] S. W. Hawking, *Phys. Rev. D* **72**, 084013 (2005), arXiv:hep-th/0507171.
- [41] A. Almheiri, D. Marolf, J. Polchinski, and J. Sully, *JHEP* **02**, 062, arXiv:1207.3123 [hep-th].
- [42] S. W. Hawking, *Phys. Lett. B* **195**, 337 (1987).
- [43] J. Maldacena and L. Maoz, *JHEP* **02**, 053, arXiv:hep-th/0401024.
- [44] G. Penington, *JHEP* **09**, 002, arXiv:1905.08255.
- [45] A. Almheiri, R. Mahajan, J. Maldacena, and Y. Zhao, *JHEP* **03**, 149, arXiv:1908.10996.
- [46] L. Susskind, *Phys. Rev. Lett.* **71**, 2367 (1993), arXiv:hep-th/9307168.
- [47] A. Strominger and C. Vafa, *Phys. Lett. B* **379**, 99 (1996), arXiv:hep-th/9601029.
- [48] A. Ashtekar and M. Bojowald, *Class. Quant. Grav.* **23**, 391 (2006), arXiv:gr-qc/0509075.
- [49] A. Perez, *Living Rev. Rel.* **16**, 3 (2013), arXiv:1205.2019 [gr-qc].
- [50] M. Reuter and F. Saueressig, *New J. Phys.* **14**, 055022 (2012), arXiv:1202.2274 [hep-th].
- [51] R. J. Adler, P. Chen, and D. I. Santiago, *Gen. Rel. Grav.* **33**, 2101 (2001), arXiv:gr-qc/0106080.
- [52] G. Amelino-Camelia, *Living Rev. Rel.* **16**, 5 (2013), arXiv:0806.0339 [gr-qc].
- [53] A. Sen, *JHEP* **04**, 156, arXiv:1205.0971 [hep-th].
- [54] A. Castro, A. Maloney, and A. Strominger, *Phys. Rev. D* **82**, 024008 (2010), arXiv:1004.0996 [hep-th].
- [55] M. Cavaglia, S. Das, and R. Maartens, *Class. Quant. Grav.* **20**, L205 (2003), arXiv:hep-ph/0305223.
- [56] K. Nozari and S. H. Mehdipour, *Class. Quant. Grav.* **25**, 175015 (2008), arXiv:0801.4074 [gr-qc].
- [57] B. J. Carr, J. Mureika, and P. Nicolini, *JHEP* **07**, 052, arXiv:1504.07637 [gr-qc].
- [58] E. W. Kolb and M. S. Turner, *The Early Universe*, *Frontiers in Physics*, Vol. 69 (Addison-Wesley, 1990).
- [59] S. Weinberg, *Cosmology* (Oxford University Press, 2008).
- [60] J. H. MacGibbon and B. R. Webber, *Phys. Rev. D* **41**, 3052 (1990).
- [61] R. Anantua, R. Easther, and J. T. Giblin, *Phys. Rev. Lett.* **103**, 111303 (2009), arXiv:0812.0825 [astro-ph].
- [62] T. Papanikolaou, V. Vennin, and D. Langlois, *JCAP* **03**, 053, arXiv:2010.11573 [astro-ph.CO].
- [63] B. P. Abbott *et al.* (LIGO Scientific, Virgo), *Phys. Rev. Lett.* **116**, 061102 (2016), arXiv:1602.03837 [gr-qc].
- [64] B. P. Abbott *et al.* (LIGO Scientific, Virgo), *Phys. Rev. X* **9**, 031040 (2019), arXiv:1811.12907 [astro-ph.HE].
- [65] J. Aasi *et al.* (LIGO Scientific), *Class. Quant. Grav.* **32**, 074001 (2015), arXiv:1411.4547 [gr-qc].
- [66] NANOGrav Collaboration, *Astrophys. J. Lett.* **951**, L8 (2023), arXiv:2306.16213.
- [67] M. E. Gertsenshtein, *Sov. Phys. JETP* **14**, 84 (1962).
- [68] A. M. Cruise and R. M. J. Ingley, *Class. Quant. Grav.* **23**, 6185 (2006).
- [69] V. Domcke and C. Garcia-Cely, *Phys. Rev. Lett.* **126**, 021104 (2021), arXiv:2006.01161 [astro-ph.CO].
- [70] Y. Chen, J. Shu, X. Xue, Q. Yuan, and Y. Zhao, *Phys. Rev. Lett.* **124**, 061102 (2020), arXiv:1905.02213 [hep-ph].
- [71] A. Berlin, N. Blinov, G. Krnjaic, P. Schuster, and N. Toro, *Phys. Rev. D* **99**, 075001 (2019), arXiv:1807.01730 [hep-ph].
- [72] N. Aggarwal *et al.*, *Living Rev. Rel.* **24**, 4 (2021), arXiv:2011.12414 [gr-qc].
- [73] G. Amelino-Camelia and L. Smolin, *Phys. Rev. D* **80**, 084017 (2009), arXiv:0906.3731 [astro-ph.HE].
- [74] T. Jacobson, S. Liberati, and D. Mattingly, *Annals Phys.* **321**, 150 (2006), arXiv:astro-ph/0505267.
- [75] P. Nicolini, A. Smalagic, and E. Spallucci, *Phys. Lett. B* **632**, 547 (2006).
- [76] P. Nicolini, *J. Phys. A* **38**, L631 (2005), arXiv:hep-th/0507266.
- [77] L. Modesto, *Class. Quant. Grav.* **23**, 5587 (2006).
- [78] A. Ashtekar and M. Bojowald, *Class. Quant. Grav.* **22**, 3349 (2005), arXiv:gr-qc/0504029.
- [79] C. Rovelli and F. Vidotto, *Int. J. Mod. Phys. D* **23**, 1442026 (2014).
- [80] S. Weinberg, ULTRAVIOLET DIVERGENCES IN QUANTUM THEORIES OF GRAVITATION, in *General Relativity: An Einstein Centenary Survey*, edited by S. W. Hawking and W. Israel (Cambridge University Press, 1979) pp. 790–831.
- [81] M. Reuter, *Phys. Rev. D* **57**, 971 (1998), arXiv:hep-th/9605030.
- [82] A. Bonanno and M. Reuter, *Phys. Rev. D* **62**, 043008 (2000).
- [83] G. T. Horowitz and J. Polchinski, *Phys. Rev. D* **55**, 6189 (1997).
- [84] D. Amati, M. Ciafaloni, and G. Veneziano, *Phys. Lett. B* **216**, 41 (1989).
- [85] J. J. Atick and E. Witten, *Nucl. Phys. B* **310**, 291 (1988).
- [86] M. K. Parikh and F. Wilczek, *Phys. Rev. Lett.* **85**, 5042 (2000), arXiv:hep-th/9907001.
- [87] M. K. Parikh, *Int. J. Mod. Phys. D* **13**, 2351 (2004), arXiv:hep-th/0405160.
- [88] A. J. M. Medved, *Phys. Rev. D* **66**, 124009 (2002), arXiv:hep-th/0207247.
- [89] A. A. Starobinsky, *Sov. Phys. JETP* **37**, 28 (1973).
- [90] S. A. Teukolsky, *Astrophys. J.* **185**, 635 (1973).
- [91] D. N. Page, *Phys. Rev. D* **14**, 3260 (1976).
- [92] D. N. Page, *Phys. Rev. D* **16**, 2402 (1977).
- [93] R. Dong, W. H. Kinney, and D. Stojkovic, *JCAP* **10**, 034, arXiv:1511.05642 [astro-ph.CO].
- [94] K. Inomata, M. Kawasaki, K. Mukaida, T. Terada, and T. T. Yanagida, *Phys. Rev. D* **101**, 123533 (2020).
- [95] L. A. Boyle and P. J. Steinhardt, *Phys. Rev. D* **77**, 063504 (2008), arXiv:astro-ph/0512014.
- [96] S. Kuroyanagi, K. Nakayama, and S. Saito, *Phys. Rev. D* **84**, 123513 (2011), arXiv:1110.4169 [astro-ph.CO].
- [97] A. E. Nelson and C. Prescod-Weinstein, *Phys. Rev. D* **96**, 113007 (2017), arXiv:1708.00010 [hep-ph].
- [98] A. Ireland, S. Profumo, and J. Scharnhorst, *Phys. Rev. D* **107**, 104021 (2023), 2302.10188.
- [99] B. Spokoiny, *Phys. Lett. B* **315**, 40 (1993).
- [100] M. Joyce, *Phys. Rev. D* **55**, 1875 (1997), arXiv:hep-ph/9606223.

- [101] D. G. Figueroa and E. H. Tanin, *JCAP* **10**, 050, arXiv:1811.04093 [astro-ph.CO].
- [102] R. T. Co, E. Gonzalez, and K. Harigaya, *JCAP* **11**, 038, arXiv:2007.04328 [astro-ph.CO].
- [103] M. Giovannini, *Phys. Rev. D* **58**, 083504 (1998), arXiv:hep-ph/9806329.
- [104] H. Tashiro, T. Chiba, and M. Sasaki, *Class. Quant. Grav.* **21**, 1761 (2004), arXiv:gr-qc/0307068.
- [105] S. Hannestad, *Phys. Rev. D* **70**, 043506 (2004), arXiv:astro-ph/0403291.
- [106] R. Easther and E. A. Lim, *JCAP* **04**, 010, arXiv:astro-ph/0601617.
- [107] J. Garcia-Bellido and D. G. Figueroa, *Phys. Rev. Lett.* **98**, 061302 (2007), arXiv:astro-ph/0701014.
- [108] R. J. Scherrer and M. S. Turner, *Phys. Rev. D* **31**, 681 (1985).
- [109] C. Caprini and D. G. Figueroa, *Class. Quant. Grav.* **35**, 163001 (2018), arXiv:1801.04268 [astro-ph.CO].
- [110] G. Domenech, *Universe* **7**, 398 (2021), arXiv:2109.01398 [gr-qc].
- [111] R. H. Cyburt, B. D. Fields, K. A. Olive, and T.-H. Yeh, *Rev. Mod. Phys.* **88**, 015004 (2016), arXiv:1505.01076 [astro-ph.CO].
- [112] N. Aghanim *et al.* (Planck), *Astron. Astrophys.* **641**, A6 (2020), [Erratum: *Astron. Astrophys.* 652, C4 (2021)], arXiv:1807.06209 [astro-ph.CO].
- [113] M. Punturo, M. Abernathy, F. Acernese, B. Allen, N. Andersson, K. G. Arun, F. Barone, B. Barr, M. Barsuglia, M. Beker, *et al.*, *Class. Quant. Grav.* **27**, 194002 (2010).
- [114] D. Reitze *et al.*, *Bull. Am. Astron. Soc.* **51**, 035 (2019), arXiv:1907.04833 [astro-ph.IM].
- [115] A. Romanenko, R. Pilipenko, S. Zorzetti, D. Frolov, M. Awida, S. Belomestnykh, S. Posen, and A. Grassellino, *Phys. Rev. Applied* **13**, 034032 (2020), arXiv:1810.03703 [quant-ph].
- [116] C. M. Caves, *Phys. Rev. D* **26**, 1817 (1982).
- [117] K. M. Backes *et al.*, *Nature* **590**, 238 (2021), arXiv:2008.01853.
- [118] L. Brouwer *et al.* (DMRadio), *Phys. Rev. D* **106**, 103008 (2022), arXiv:2204.13781 [hep-ex].
- [119] A. D. Ludlow, M. M. Boyd, J. Ye, E. Peik, and P. O. Schmidt, *Rev. Mod. Phys.* **87**, 637 (2015), arXiv:1407.3493.

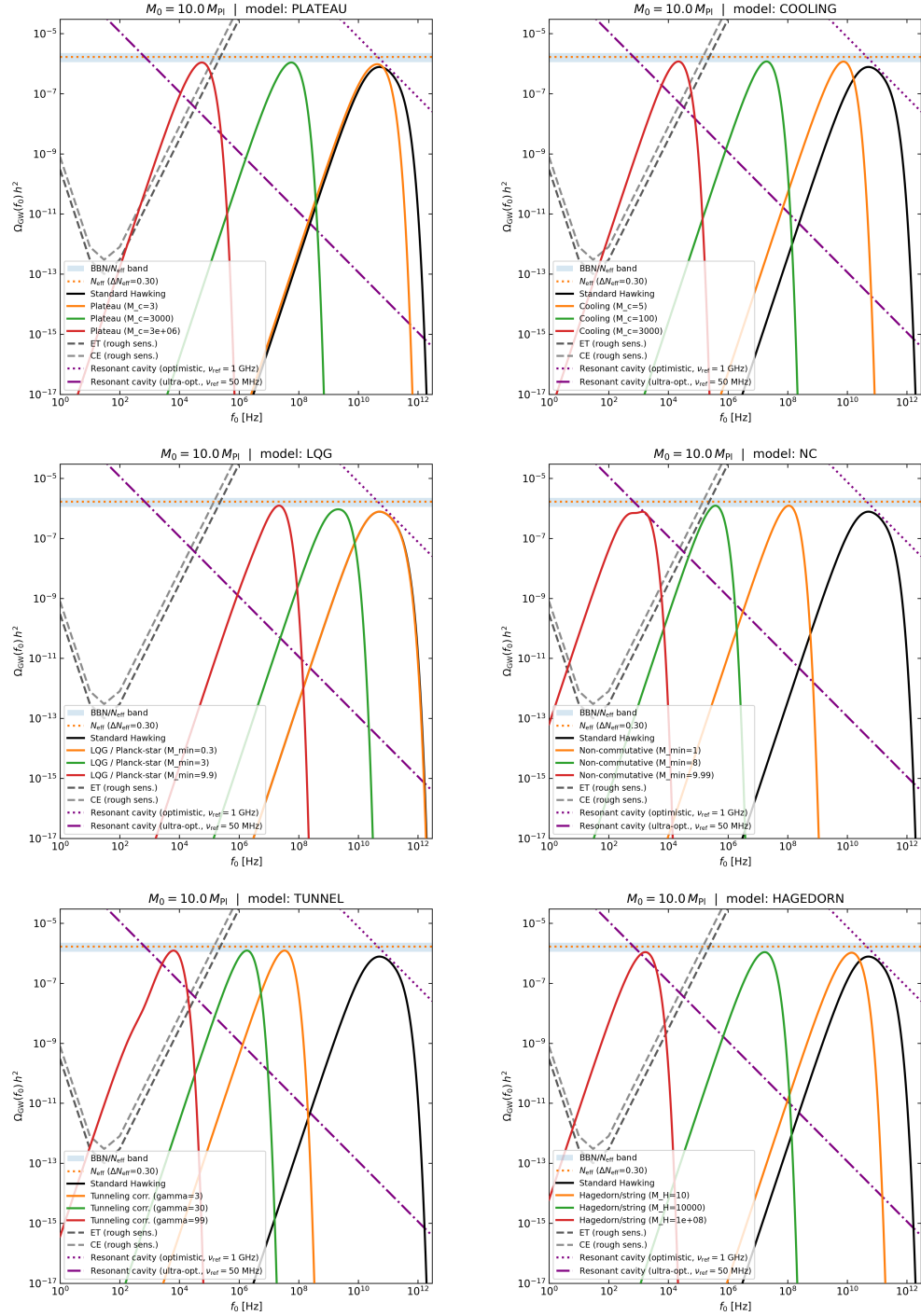


FIG. 4. Gravitational wave energy density spectra $\Omega_{\text{GW}}(f_0) h^2$ from primordial black hole evaporation for six modified Hawking temperature models, computed for $M_0 = 10 M_{\text{Pl}}$. Each panel shows the standard Hawking result (black solid) alongside three representative parameter choices for: Plateau suppression (top left, $M_c = 3, 3000, 3 \times 10^6$), Cooling (top right, $M_c = 5, 100, 3000$), LQG/Planck-star (middle left, $M_{\text{min}} = 0.3, 3, 9.9$), Non-commutative geometry (middle right, $M_{\text{min}} = 1, 8, 9.99$), Tunneling corrections (bottom left, $\gamma = 3, 30, 99$), and Hagedorn/string-inspired (bottom right, $M_H = 10, 10^4, 10^8$). All spectra are normalized to $\Delta N_{\text{eff}} = 0.3$; the corresponding BBN/ N_{eff} constraint band is shown in light blue with the central value indicated by an orange dotted line. Also shown for reference are approximate power-law sensitivity curves for the Einstein Telescope (ET, dark gray dashed) and Cosmic Explorer (CE, light gray dashed), and two resonant-cavity sensitivity projections: an optimistic scenario with $\nu_{\text{ref}} = 1$ GHz (purple dotted) and an ultra-optimistic scenario with $\nu_{\text{ref}} = 50$ MHz (purple dot-dashed). Increasing the model-specific cutoff parameter generically shifts the spectral peak to lower frequencies and suppresses high-frequency emission relative to the standard Hawking case.

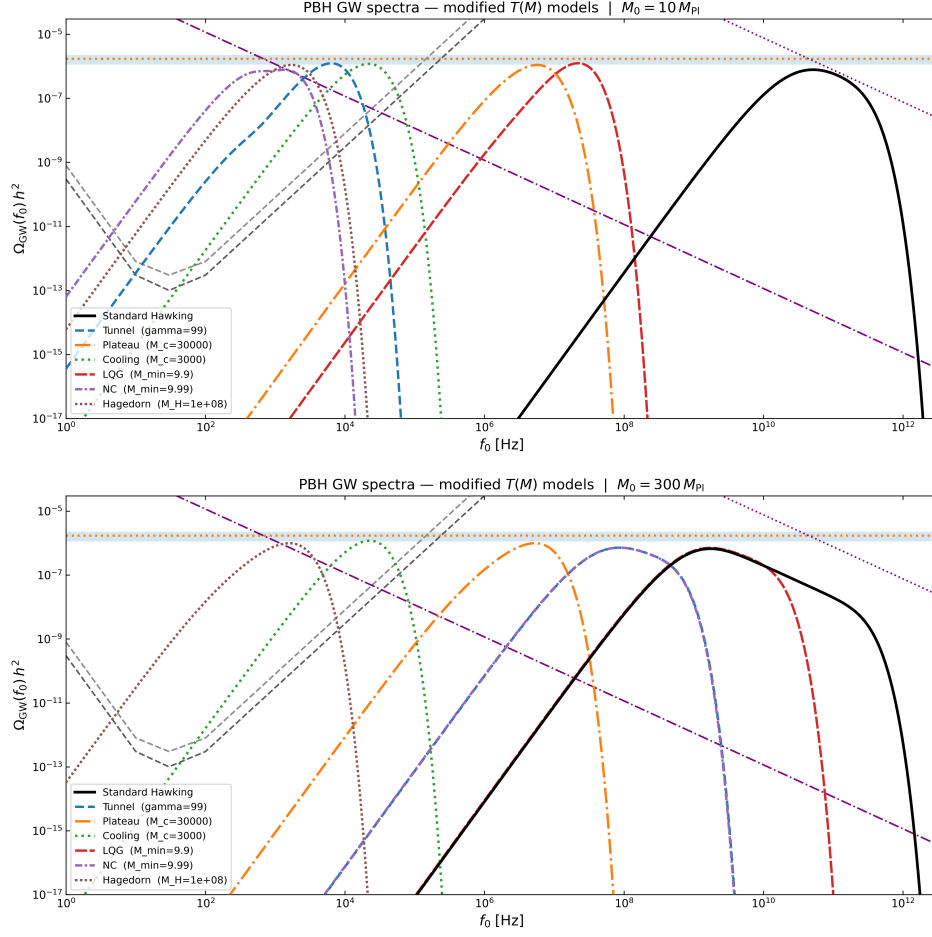


FIG. 5. Gravitational wave energy density spectra $\Omega_{\text{GW}}(f_0) h^2$ from primordial black hole evaporation for six modified Hawking temperature models, shown for two initial masses: $M_0 = 10 M_{\text{Pl}}$ (top) and $M_0 = 300 M_{\text{Pl}}$ (bottom). In each panel the standard Hawking result is shown as a black solid curve, with the following modified-temperature models overlaid: Tunneling corrections ($\gamma = 99$, blue dashed), Plateau suppression ($M_c = 3 \times 10^4$, orange dot-dashed), Cooling ($M_c = 3000$, green dotted), LQG/Planck-star ($M_{\text{min}} = 9.9$, red dense-dashed), Non-commutative geometry ($M_{\text{min}} = 9.99$, purple dash-dot-dot), and Hagedorn/string-inspired ($M_H = 10^8$, brown dense-dotted). All spectra are normalized to $\Delta N_{\text{eff}} = 0.3$; the BBN/ N_{eff} constraint band is shown in light blue with the central value ($\Delta N_{\text{eff}} = 0.30$) indicated by an orange dotted line. Gray dashed curves show approximate power-law sensitivity envelopes for the Einstein Telescope (ET, dark gray) and Cosmic Explorer (CE, light gray); purple dotted and dot-dashed curves show resonant-cavity sensitivity projections for optimistic ($\nu_{\text{ref}} = 1 \text{ GHz}$) and ultra-optimistic ($\nu_{\text{ref}} = 50 \text{ MHz}$) configurations, respectively. Increasing M_0 shifts all spectral peaks to lower frequencies, while the relative displacement between the standard Hawking peak and those of the modified models reflects the characteristic mass scale introduced by each scenario.

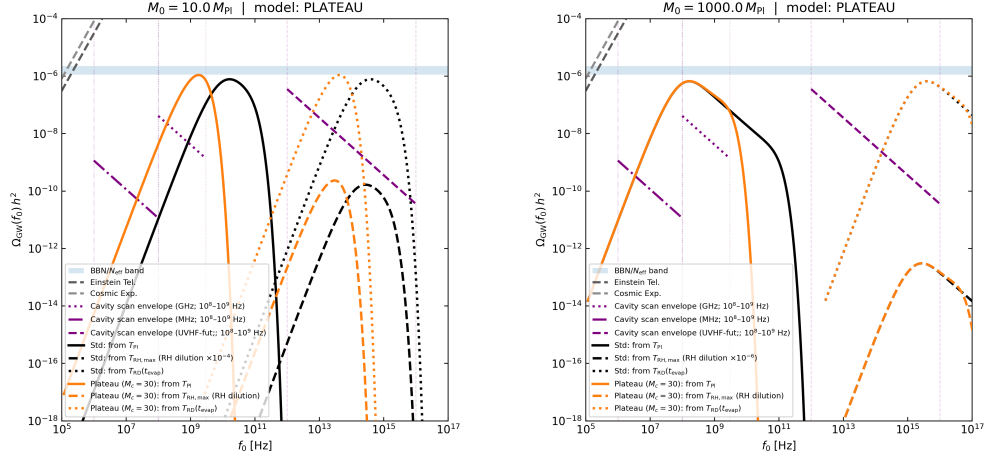


FIG. 6. Gravitational wave energy density spectra $\Omega_{\text{GW}}(f_0) h^2$ from primordial black hole evaporation for the Plateau temperature model ($M_c = 30$), shown for two initial masses: $M_0 = 10 M_{\text{Pl}}$ (left) and $M_0 = 1000 M_{\text{Pl}}$ (right). In each panel the standard Hawking result is shown as a solid black curve. Orange curves show the Plateau model ($M_c = 30$) under three cosmological redshifting assumptions: emission from T_{RH} (solid), emission from $T_{\text{RH,max}}$ with RH dilution (dashed), and emission from $T_{\text{RH}}(f_{\text{max}})$ (dotted). Black dashed and dotted curves show the corresponding standard Hawking spectra under the same redshifting scenarios (with RH dilution $\times 10^{-5}$ as noted). All spectra are normalized to $\Delta N_{\text{eff}} = 0.3$; the BBN/ N_{eff} constraint band is shown in light blue. Also shown are approximate power-law sensitivity envelopes for the Einstein Telescope (ET, dark gray dashed) and Cosmic Explorer (CE, light gray dashed), and resonant-cavity sensitivity projections for GHz-scale (purple dotted, 10^8 – 10^9 Hz), MHz-scale (purple dot-dashed, 10^6 – 10^8 Hz), and UVHF (purple dashed, 10^{12} – 10^{16} Hz) configurations. Increasing M_0 shifts all spectral features to lower frequencies, while different reheating assumptions can displace the peak by many decades, illustrating the degeneracy between the black-hole temperature model and the cosmological expansion history.